ACOUSTIC WAVE PROPAGATION AND INTENSITY FLUCTUATIONS IN SHALLOW WATER 2006 EXPERIMENT

by

Jing Luo

A thesis submitted to the Faculty of the University of Delaware in partial fulfillment of the requirements for the degree of Master of Science in Electrical & Computer Engineering

Summer 2016

© 2016 Jing Luo
All Rights Reserved

ProQuest Number: 10191348

All rights reserved

INFORMATION TO ALL USERS
The quality of this reproduction is dependent upon the quality of the copy submitted.

In the unlikely event that the author did not send a complete manuscript
and there are missing pages, these will be noted. Also, if material had to be removed,
a note will indicate the deletion.

ProQuest 10191348

Published by ProQuest LLC (2016). Copyright of the Dissertation is held by the Author.

All rights reserved.
This work is protected against unauthorized copying under Title 17, United States Code
Microform Edition © ProQuest LLC.

ProQuest LLC.
789 East Eisenhower Parkway
P.O. Box 1346
Ann Arbor, MI 48106 - 1346

ACOUSTIC WAVE PROPAGATION AND INTENSITY FLUCTUATIONS IN SHALLOW WATER 2006 EXPERIMENT

by

Jing Luo

Approved: _____

Mohsen Badiey, Ph.D.
Professor in charge of thesis on behalf of the Advisory Committee

Approved: _____

Kenneth E. Barner, Ph.D.
Chair of the Department of Electrical & Computer Engineering

Approved: _____

Babatunde A. Ogunnaike, Ph.D.
Dean of the College of Engineering

Approved: _____

Ann L. Ardis, Ph.D.
Senior Vice Provost for Graduate & Professional Education

ACKNOWLEDGMENTS

I wish to thank my adviser, Mohsen Badiey for introducing me to the field of Shallow Water Acoustical Oceanography and providing opportunities for me to participate in several field experiments. Through these sea going activities I learned a lot about data acquisition at sea and about instrumentation and signal processing. His continuous support during my research at the University of Delaware is appreciated. I also want to thank my friends and colleagues Justin Eickmeier, Lin Wan and Entin Karjadi, and all the participants of the Shallow Water 2006 (SW06) experiment for helping in the experiment and numerous insightful discussions. I am also indebted to my spouse, Yan Lin, without whom this would ever have been possible. Her patience and endurance during my studies is greatly appreciated.

TABLE OF CONTENTS

LIST OF TABLES . . . . . **vi**
LIST OF FIGURES . . . . . **vii**
ABSTRACT . . . . . **xii**

Chapter

1 INTRODUCTION **1**

1.1 Nonlinear Internal Waves in Shallow Water Region 1
1.2 Broadband Acoustic Wave Propagation in Shallow Water . . . 2
1.3 Outline of Thesis 6

2 SHALLOW WATER WAVEGUIDE **7**

2.1 Linear Wave Equation and Helmholtz Equation 7
2.2 Normal-Mode Method 8
2.3 Horizontal Refraction Equation 11
2.4 Parabolic Equation Method 12

3 SHALLOW WATER 2006 EXPERIMENT AND OCEANOGRAPHIC MEASUREMENT **14**

3.1 Internal Wave Observation 17

3.1.1 Internal Wave Event on Aug. 17th, 2006 19
3.1.2 Characteristics of the Internal Wave Packet 21

3.2 Acoustic Moorings 24

3.2.1 Underwater Acoustic Source 24

3.2.2 Underwater Acoustic Receiver Array 25

3.3 Reconstruction of Three Dimensional NIW Environment . . . 26

4 ACOUSTIC OBSERVATION AND MODELING IN THE INTERNAL WAVE EVENT 31

4.1 Acoustic Transmission Received on Shark Array 32

4.1.1 Transmission 21:00-21:07GMT 35
4.1.2 Transmission 21:30-21:37GMT 38
4.1.3 Transmission 22:00-22:07GMT 40
4.1.4 Transmission 22:30-22:37GMT 43

4.2 Horizontal Lloyd's Mirror Effect 46

4.2.1 Two-Dimensional Model 47
4.2.2 Three-Dimensional Model 52

5 SUMMARY 60

BIBLIOGRAPHY 62

LIST OF TABLES

1.1 Researches on internal waves' impact on acoustic transmission. 5

3.1 Direction and speed of the internal wave packet on Aug. 17, 2006. 22

3.2 Transmitted signals from fixed(NRL300) source 25

3.3 Acoustic transmission during NIW event on Aug. 17, 2006 . 25

3.4 Local velocity and direction of the internal wave packet on Aug. 17, 2006. 29

4.1 Summary of transmission schedule during geotimes Tg_1 to Tg_4 listing the distance between the NIW front to the acoustic track. (Distances are in km. Positive distance indicates the leading NIW front is at the south-east side of the acoustic track, negative distance indicates the front is at the north-west side of the acoustic track) 33

LIST OF FIGURES

1.1 Horizontal and vertical views of internal solitary waves. In horizontal view, R_c radius of wave front for cylindrical expansion, D internal wave length. In vertical view, η_0 vertical displacement, L length of wave packet. 4

3.1 Map of SW06 experiment site and the locations of the environment and acoustic moorings 15

3.2 Current data record by ADCP at mooring SW32 on Aug.17, 2006(upper panel) and temperature data at the same location. 16

3.3 Image of SW06 experiment site taken by the Canadian RADARSAT satellite on 16 August, 2006. Bathymetric contours are overlaid and the positions of Shark VHLA and NRL300 sources are shown. 18

3.4 Depth of 18^oC degree isotherm on Aug. 17, 2006, recorded on WHOI Sharp VLA (SW54) 19

3.5 Angular distribution of the direction of the internal wave recored during SW06. 20

3.6 Diagram showing the fixed acoustic source(NRL300), receiver array (Shark VHLA) and the semi-circular track of R/V Sharp the IW on Aug. 17, 2006. 21

3.7 Time series of vertical displacement of internal wave at depth = 20, 30, 40 and 50 m, Aug. 7th - 8th. The depression is 15-20 m at different depths, and generally return to mean level. The greatest amplitude is measured at about 30 m, coincident with the location of the thermocline. 23

3.8 Time series of vertical displacement of internal wave (same measuring condition as in Fig.3.7 but filtered with a high-pass filter. 24

3.9 Depth-temperature plot from J15 temperature sensor data collected from 23:22:50-23:31:00, June 22. Data shows for the first 13m, the sea water is well mixed and the temperature is constant $\sim 25^oC$. 27

3.10 Combined radar images from R/V Sharp(blue) and R/V Oceanus(black). Blue and pink lines show their ship tracks during the internal wave event on Aug. 17, 2006. A red dashed line outlines one possible shape of the leading fronts. 28

3.11 Reconstructed environment at 21:30:00, Aug. 17th (Depth = 15m). The temperature matches well with the curved internal wave fronts from two radar images. 30

4.1 Received chirp signal on Shark array at GMT15:57:04, Aug 03rd, (a)before and (b)after matched filtering. 32

4.2 Schematic diagram showing the geometry of the fixed sound source (point B) and receiver array (point A) and the NIW soliton approaching at angle of α between its straight line wave front and acoustic track AB. Mooring SW32 (point C) was located at the midle to provide additional temperature measurement. 33

4.3 Temperature profiles measured at (A) the acoustic source, (B) at the shark VLA array, and (C) the midpoint between the source and receiver during August 17, 2006 from 20.00 to 23:00 GMT. The geotime intervals Tg_1 through Tg_4 are tabulated in Table 4.1. For the shallow water region, with small changes to the salinity profile, we consider the temperature profile to be representing the behavior of the sound speed profile (SSP). For each sub plot, the SSP profiles for the four geotimes are shown on the right panel indicating the dynamic behavior of the thermocline. 34

4.4 Positions of the acoustic receiver (A), source (B), and a thermistor chain in the mid-point (C) at Tg_1 (21:00 GMT). (b) Geotime-Frequency spectrogram showing the received signal from 21:00 to 21:07 GMT. (C) Signal intensity versus geotime in depth. Blue line is the depth integrated intensity. (d) First six modes filtered using modal decomposition. . . . 37

4.5 Positions of the acoustic receiver (A), source (B), and a thermistor chain in the mid-point (C) at Tg_2 (21:30 GMT). (b) Geotime-Frequency spectrogram showing the received signal from 21:30 to 21:37 GMT. (C) Signal intensity versus geotime in depth. Blue line is the depth integrated intensity. (d) First six modes filtered using modal decomposition. . . . 39

4.6 (a) The position of the NIW soliton front before it arrives at acoustic track AB. (b) The position of the NIW soliton front before it arrives at acoustic track AB. 40

4.7 Positions of the acoustic receiver (A), source (B), and a thermistor chain in the mid-point (C) at Tg_3 (22:00 GMT). (b) Geotime-Frequency spectrogram showing the received signal from 22:00 to 22:07 GMT. (C) Signal intensity versus geotime in depth. Blue line is the depth integrated intensity. (d) First six modes filtered using modal decomposition. . . . 42

4.8 Positions of the acoustic receiver (A), source (B), and a thermistor chain in the mid-point (C) at Tg_4 (22:30 GMT). (b) Geotime-Frequency spectrogram showing the received signal from 22:30 to 22:37 GMT. (C) Signal intensity versus geotime in depth. Blue line is the depth integrated intensity. (d) First six modes filtered using modal decomposition. . . . 45

4.9 Geotime-frequency striations at different time during SW06 experiment at GMT20:30-22:37,Aug 17th(top row), GMT10:00-12:07, Aug 18th(middle row) and GMT10:00-12:07, Aug 19th(bottom row). 46

4.10 Temperature data recorded on (a) the acoustic source and (b) on the Shark VLA receiver from 20:30 to 23:30GMT, on Aug 17th, 2006. The start and end time of the transmission session are marked by two dashed lines. (c) Depth-averaged intensity of received LFM chirps on the Shark VLA hydrophone array during the transmission session from 21:30 to 21:37GMT. (d) Averaged spectrogram of received LFM signal. 48

4.11 Diagram of source-receiver track relative to the leading internal wave front moving at speed = v. r_1 is the direct path, r_2 is the refracted path, and r_2' is reflected path under the two-layer assumption. 50

4.12 Simulated acoustic spectrogram and intensity as a function of geotime. (a) Spectrogram using two-layer assumption [Eq.4.3]. (b) Intensity of a broadband LFM signal (270-330Hz) using two-layer assumption [Eq.4.4]; (c) Period and slope of the interference pattern [Eq.4.7 and 4.11]. (d) Spectrogram from 3D PE model. (e) Intensity of a broadband LFM signal (270-330Hz) from 3D PE model. . . 53

4.13 Left panel: Horizontal ray plot showing the effects of the incoming internal wave front on the propagation of vertical modes 1-3 (from top to bottom). Three red lines show the front, center, back of the incoming internal wave. Right panel: Geo-time as a function of arrival time of the first three modes (from top to bottom). The horizontal blue lines in each subplot indicate the geo-times, respectively. 55

4.14 From top to bottom, PE modeling results of mode 1-3. The impacts of an incoming internal wave packet are different depending on the mode. 57

4.15 PE modeling with realistic environment matching observed acoustic mechanisms in event 50. (A) Horizontal Lloyd mirror effect using reconstructed environment. (B) Focusing/defocusing event using reconstructed environment matching observations in SW06 experiment. 58

4.16 Comparison of vertical modes intensity. Left column: modal decomposition of recieved acoustic data on Shark array. Right column: PE model results of single mode propagation with realistic environment input. 59

ABSTRACT

Fluctuations of low frequency sound propagation in the presence of nonlinear internal waves during the Shallow Water 2006 experiment are analyzed. Acoustic waves and environmental data including on-board ship radar images were collected simultaneously before, during, and after a strong internal solitary wave packet passed through a source-receiver acoustic track. Analysis of the acoustic wave signals shows temporal intensity fluctuations. These fluctuations are affected by the passing internal wave and agrees well with the theory of the horizontal refraction of acoustic wave propagation in shallow water. The intensity focusing and defocusing that occurs in a fixed source-receiver configuration while internal wave packet approaches and passes the acoustic track is addressed in this thesis.

Acoustic ray-mode theory is used to explain the modal evolution of broadband acoustic waves propagating in a shallow water waveguide in the presence of internal waves. Acoustic modal behavior is obtained from the data through modal decomposition algorithms applied to data collected by a vertical line array of hydrophones.

Strong interference patterns are observed in the acoustic data, whose main cause is identified as the horizontal refraction referred to as the horizontal Lloyd mirror effect. To analyze this interference pattern, combined Parabolic Equation model and Vertical-mode horizontal-ray model are utilized. A semi-analytic formula for estimating the horizontal Lloyd mirror effect is developed.

Chapter 1

INTRODUCTION

Underwater acoustic propagation has been an active research field for more than a century. Originated from military purposes, its applications have expanded to other areas such as environmental monitoring, navigation and underwater communication in modern era. Scientists have made great advances in understanding the theory by developing modeling tools for underwater wave propagation. However, shallow water environment still remains a challenging problem due to complex temporal and spacial variability of sound speed profile (SSP) that is primarily driven by the oceanographic conditions of these regions. In this research, we define some dominant oceanographic phenomenon such as the nonlinear internal wave (NIW) in shallow water and its effect on the propagation of broadband acoustic signals. We then show results from our recent field observations conducted on the New Jersey continental shelf and present the supporting analysis showing the cause and effect between the intensity fluctuations of the sound wave and variability of the sound speed profile stemming from the oceanography in the region.

1.1 Nonlinear Internal Waves in Shallow Water Region

Internal waves are generated by a strong density stratification of water temperature and salinity in shallow water regions at the bottom of surface mixed layer ($\sim$ i.e. 15 - 40m below sea surface). A typical internal wave with description of the parameters presented in horizonal and vertical views

is shown in Fig.1.1 by Apel [1]. The tidal interaction with bottom feature (e.g., shelf break) appears to be the dominant mechanism for generation of the internal waves near the continents. These nonlinear waves have been observed by scientists around 19th century. Theoretical explanation of these waves was initially given by Boussinesq and Rayleigh in 1870s, and later by Korteweg and de Vries in 1895 [2]. More recent studies indicate interests in this phenomenon and the effects that it can have in sound wave propagation. For example, Ostrovsky and Stepanyants[3], Apel[4], Duda and Farmer[5], Badiey *et al.*.[6, 7, 8] have all used different aspects of these waves in recent years. Nonlinear internal waves that occur in depths below sea surface can also be observed on the sea surface by radar.

The interaction between NIW and propagation of sound simultaneously in water column has recently been of interest.

1.2 Broadband Acoustic Wave Propagation in Shallow Water

Shallow water regions provide a waveguide for the acoustic waves to propagate. These waves interact with the waveguide boundaries (i.e., sea surface and sea bottom), as well as the water column. Changes of sound speed profile in water column and the reflectivity index of the boundaries can substantially change the intensity of sound propagating in shallow water waveguide. Complexity in these parameters presents a challenge to interpret a received sound signal that has passed through the waveguide. Original work in shallow water waveguides goes back to Pekeris, Ewing, and Worzel[9]. And the problem is known classically as Pekeris waveguide. For simple SSP, the acoustic wave equation reduces to a set of differential equations with constant coefficients yielding a closed form solution known as model theory of waveguides. However, the variable SSP presents nontrivial and sometimes complex

solution for the acoustic wave equation. The passing nonlinear internal wave in shallow water causes the SSP to vary substantially and hence will effect the intensity of acoustic wave propagation. In 1991, Zhou *et al.*[10] reported the effect of nonlinear internal wave in Yellow Sea experiment on acoustic waves causing high propagation intensity loss up to 30-40dB. These high losses were attributed to Bragg resonant scattering when acoustic signal travels through a strong internal wave train. Another proposed mechanism shown by Preisig and Duda [11] through numerical simulation is coupled mode theory, which proposed mode-coupling to be the reason.

The problem of acoustic wave propagation in presence of NIW has recently been studied both experimentally [12, 11, 13, 6, 14] and theoretically[15, 16, 17, 18] by several investigators.

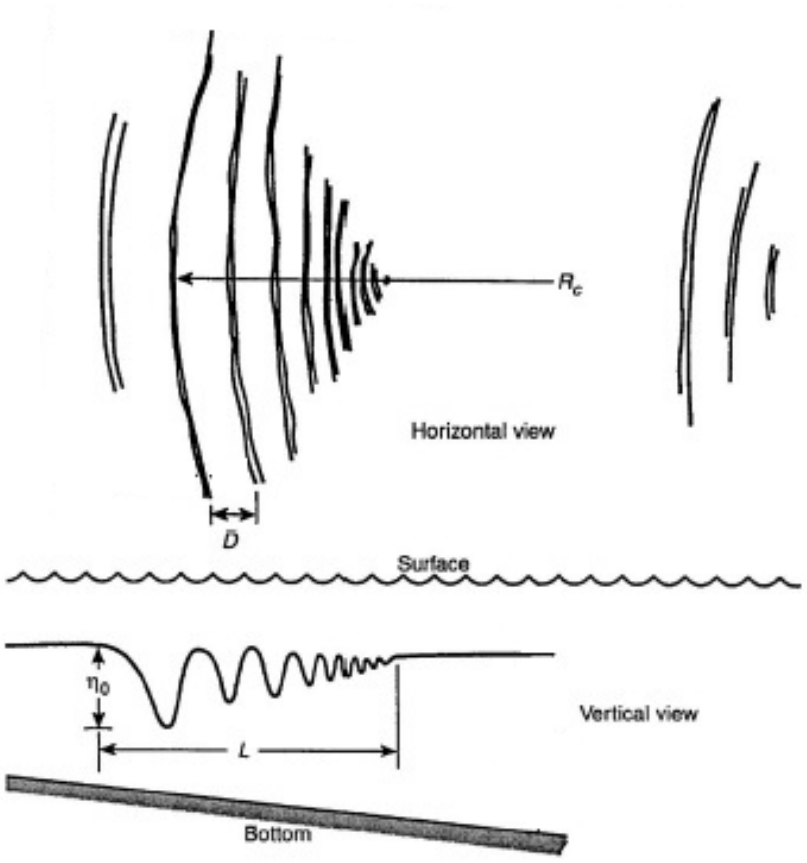

Figure 1.1: Horizontal and vertical views of internal solitary waves. In horizontal view, R_c radius of wave front for cylindrical expansion, D internal wave length. In vertical view, η_0 vertical displacement, L length of wave packet.

Experiment	**Waveguide**	**Internal waves**	**Signal**	**Results**
Zhou *et al.* (1991) [10]	Yellow sea L= 28 km; D=40 m	Hypothesized $\alpha > 45^o$	Broadband 100-1000 Hz	Freq. fluct. >20 dB Resonant mode Coupling
Rubenstein & Brill,(1991)[12]	Washington coast L=18.5km; D=150m	N$\sim$ 10 cph Ampl $\sim 10m$ $\alpha \sim 10-15^o$	Narrowband f = 400 Hz	Temp. intens. fluct.$\sim 3dB$ Adiabatic fluctuations
Rubenstein, D. (1999)[13]	Gulf of Mexico L= 30km; D=185m	N: 15-20cph Ampl$\sim$ $10m$ $\alpha \sim 30^o$	Narrowband f = 240 Hz	Temp. intens. fluct.$\sim 2dB$ Mode coupling
Badiey, Lynch, et al. (2002)[6]	New Jersey shelf L=15 km; D=70 m	N: 10-15cph Ampl$\sim$ $12m\alpha \sim 5^o$	Broadband 30-160 Hz and LFM 50-250 Hz	Space-time int. fluct.$\sim 6-7dB$ 3D effects (horizontal refraction)
Badiey, Lynch, et al. (2002)[6]	New Jersey shelf L=19 km; D=70-100m	N: 10-15cph Ampl$\sim$ $12m$ $\alpha \sim 35-40^o$	Broadband 30-160 Hz and LFM 50-250 Hz	Space-time int. fluct.$\sim 2-3dB$ Mode coupling
Badiey, Katsnelson,*et al.*(2005)[7]	New Jersey shelf L=15 km; D=70 m	N: 10-15 cph Ampl$\sim$ $12m$ $\alpha \sim 5^o$	Broadband 30-160 Hz	Space-time int. fluct.$\sim 6-7dB$ 3D effects Frequency dependence
Luo, Badiey,*et al.*(2008)[14]	New Jersey shelf L=20 km; D=70 m	N: 10-15 cph Ampl$\sim$ $12m$ $\alpha \sim 3^o-5^o$	Broadband 270-330 Hz	Space-time int. fluct.$\sim 15dB$ 3D effects Frequency dependence
J. Lynch, C. Emerson, *et al.*(2012)[19]	New Jersey shelf	full circle	low frequency (600, 900Hz)	space-time fluct. 3D effects

Table 1.1: Researches on internal waves' impact on acoustic transmission.

Table 1.1 provides a summary of some recent studies showing acoustic wave propagation in shallow water in the presence of NIW with parameters including source-receiver range, water depth and the acoustic frequency. In addition, in Table 1.1, the orientation between acoustic track and NIW wave front is listed. It is shown that large acoustic intensity fluctuations of about 15dB can result from a small azimuthal angle between NIW and acoustic track.

1.3 Outline of Thesis

Chapter 2 discusses the basic theory of acoustic wave propagation in shallow water waveguide, and introduces the theory of normal mode propagation. This chapter also includes a brief review of the vertical mode and horizontal ray theory and the Parabolic Equation (PE) solution.

Chapter 3 discusses a recent experiment and the collected data used in this thesis. Simultaneous acoustic and oceanographic data collected during the experiment were processed and later reconstructed as input for the three dimensional numerical models.

In chapter 4 the analysis of the acoustic signal received in the experiment for a specific NIW event is presented. Acoustic data are modeled and the phenomenon of horizontal refraction is explained.

In chapter 5 summary and conclusions of the research are provided and future investigations are outlined.

Chapter 2

SHALLOW WATER WAVEGUIDE

2.1 Linear Wave Equation and Helmholtz Equation

The detailed derivation of linear wave equation and its solutions can be found in literature. Here, we largely follow the derivation in [20]. Start from linear wave equation

$$\frac{\partial \rho'}{\partial t} = -\rho_0 \nabla \cdot \mathbf{v}, \tag{2.1}$$

$$\frac{\partial \mathbf{v}}{\partial t} = -\frac{1}{\rho_0} \nabla p'(\rho), \tag{2.2}$$

$$p' = \rho' c^2. \tag{2.3}$$

where c is the speed of sound in the fluid, ρ is the density, $\mathbf{v}$ the particle velocity, p the pressure. Small perturbations (i.e. $p\prime$ and $\rho\prime$) are used for pressure and density, $p = p_0 + p'$, $\rho = \rho_0 + \rho'$. And $\mathbf{v}$ is also a small quantity compare to c.

Rearrange Eq.2.1-Eq.2.3 to obtain a wave equation for pressure, and assuming medium density is constant,

$$\nabla^2 p - \frac{1}{c^2} \frac{\partial^2 p}{\partial t^2} = 0. \tag{2.4}$$

By using the Forier transform, the wave equation becomes the Helmholtz equation,

$$\rho \nabla \cdot \left(\frac{1}{\rho} \nabla p \right) + k(\mathbf{r})^2 p = 0, \tag{2.5}$$

or, in the case of constant density,

$$\nabla^2 p + k(\mathbf{r})^2 p = 0. \tag{2.6}$$

where $k(\mathbf{r})$ is the medium wavenumber of frequency ω,

$$k(\mathbf{r}) = \frac{\omega}{c(\mathbf{r})}. \tag{2.7}$$

2.2 Normal-Mode Method

We can solve the wave equation using the normal-mode method. In a cylindrical coordinate system $\mathbf{r} = (r, \varphi, z)$, assuming sound speed and density depending only on depth z, with a point source located at coordinates $r = 0, z = z_s$,

the Helmholtz equation:

$$\frac{1}{r}\frac{\partial}{\partial r}\left(r\frac{\partial p}{\partial r}\right) + \rho(z)\frac{\partial}{\partial z}\left(\frac{1}{\rho(z)}\frac{\partial p}{\partial z}\right) + \frac{\omega^2}{c^2(z)}p = -\frac{\delta(r)\delta(z-z_s)}{2\pi r}. \tag{2.8}$$

Equation 2.8 is readily solved via the technique of separation of variables. Assuming a solution of the unforced equation of $p(r, z) = \Phi(r)\Psi(z)$. Substituting into Eq.2.8 and dividing by $\Phi(r)\Psi(z)$,

$$\frac{1}{\Phi}\left[\frac{1}{r}\frac{d}{dr}\left(r\frac{d\Phi}{dr}\right)\right] + \frac{1}{\Psi}\left[\rho(z)\frac{d}{dz}\left(\frac{1}{\rho(z)}\frac{d\Psi}{dz}\right) + \frac{\omega^2}{c^2(z)}\Psi\right] = 0. \tag{2.9}$$

Let the separation constant be k_{rm}^2, we have the modal equation,

$$\rho(z)\frac{d}{dz}\left[\frac{1}{\rho(z)}\frac{d\Psi_m(z)}{dz}\right] + \left[\frac{\omega^2}{c^2(z)} - k_{rm}^2\right]\Psi_m(z) = 0. \tag{2.10}$$

where k_m is the mode m horizontal wavenumber, and each Ψ_m is subject to certain boundary conditions that depend on the environment. For instance, with a pressure-release surface located at $z = 0$ and a perfectly rigid bottom located at $z = D$, the corresponding boundary condition for Ψ is

$$\Psi(0) = 0, \qquad \left.\frac{d\Psi}{dz}\right|_{z=D} = 0. \tag{2.11}$$

Here, the function $\Psi_m(z)$ is an eigenfunction and k_{rm} is an eigenvalue. The modes are orthogonal, i.e.,

$$\int_0^D \frac{\Psi_m(z)\Psi_n(z)}{\rho(z)} d(z) = 0, \qquad \text{for} \qquad m \neq n. \tag{2.12}$$

We can normalize the solutions so that

$$\int_0^D \frac{\Psi_m^2(z)}{\rho(z)} dz = 1. \tag{2.13}$$

The total acoustic pressure field takes the form

$$p(r,z) = \sum_m \Phi_m(r)\Psi_m(z) \tag{2.14}$$

where $\Psi_m(z)$ is the vertical modal function, and $\Phi_m(r)$ is the mode coefficient for mode m at range r. Substitute this to Eq.2.8, we have

$$\sum_{m=1}^{\infty} \left\{ \frac{1}{r}\frac{d}{dr}\left(r\frac{d\Phi_m(r)}{dr}\right)\Psi_m(z) + \Phi_m(r)\left[\rho(z)\frac{d}{dz}\left(\frac{1}{\rho(z)}\frac{d\Psi_m(z)}{dz}\right) + \frac{\omega^2}{c^2(z)}\Psi_m(z)\right]\right\} = -\frac{\delta(r)\delta(z-z_s)}{2\pi r}. \tag{2.15}$$

Using the modal equation Eq.2.10, it can be simplified as

$$\sum_{m=1}^{\infty} \left\{ \frac{1}{r}\frac{d}{dr}\left(r\frac{d\Phi_m(r)}{dr}\right)\Psi_m(z) + k_{rm}^2\Phi_m(r)\Psi_m(z)\right\} = -\frac{\delta(r)\delta(z-z_s)}{2\pi r}. \tag{2.16}$$

Using the orthogonality property of modal function (Eq.2.12), we have for nth mode,

$$\frac{1}{r}\frac{d}{dr}\left[r\frac{d\Phi_n(r)}{dr}\right] + k_{rn}^2\Phi_n(r) = -\frac{\delta(r)\Psi_n(z_s)}{2\pi r\rho(z_s)} \tag{2.17}$$

The solution is given in terms of a Hanekl function of the first kind as

$$\Phi_n(r) = \frac{i}{4\rho(z_s)}\Psi_n(z_s)H_o^{(1)}(k_{rn}r). \tag{2.18}$$

The complete acoustic pressure at (r, z) is

$$p(r,z) = \frac{i}{4\rho(z_s)} \sum_{m=1}^{\infty} \Psi_m(z_s)\Psi_m(z) H_0^{(1)}(k_{rm} r). \tag{2.19}$$

where, $H_0^{(1)}(\cdot)$ is the Hankelfunction of the first kind. The asymptotic approximatation to the Hankel function has the form

$$H_0^{(1)}(k_{rm} r) \approx \sqrt{\frac{2}{\pi k_{rm} r}} e^{i(k_{rm} r - \frac{\pi}{2})} \tag{2.20}$$

when $k_{rm} r \gg 1$. With Eq.2.20, Eq.2.19 becomes

$$p(r,z) \approx \frac{i}{\rho(z_s)\sqrt{8\pi r}} e^{-i\pi/4} \sum_{m=1}^{\infty} \Psi_m(z_s)\Psi_m(z) \frac{e^{(ik_r m)r}}{\sqrt{k_{rm}}}. \tag{2.21}$$

For a range-dependent environment, the Helmholtz equation in cylindrical coordinates is,

$$\frac{\rho}{r}\frac{\partial}{\partial r}\left(\frac{r}{\rho}\frac{\partial p}{\partial r}\right) + \rho\frac{\partial}{\partial z}\left(\frac{1}{\rho}\frac{\partial p}{\partial z}\right) + \frac{\omega^2}{c^2(r,z)} p = -\frac{\delta(r)\delta(z - z_s)}{2\pi r}. \tag{2.22}$$

The solution can be expressed as a sum of local modes as

$$p(r,z) = \sum_m \Phi_m(r)\Psi_m(r,z) \tag{2.23}$$

where $\Psi_m(r,z)$ are the local modes defined by

$$\rho(r,z)\frac{\partial}{\partial z}\left[\frac{1}{\rho(r,z)}\frac{\partial \Psi_m(r,z)}{\partial z}\right] + \left[\frac{\omega^2}{c^2(r,z)} - k_{rm}^2(r)\right]\Psi_m(r,z) = 0. \tag{2.24}$$

Substitution in the Helmholtz equation yields

$$\sum_m \frac{\rho}{r}\frac{\partial}{\partial r}\left(\frac{r}{\rho}\frac{\partial(\Phi_m\Psi_m)}{\partial r}\right) + \sum_m k_{rm}^2(r)\Phi_m\Psi_m = -\frac{\delta(r)\delta(z - z_s)}{2\pi r}. \tag{2.25}$$

Assuming that ρ is independent of r. We can apply the operator

$$\int (\cdot)\frac{\Psi_n(r,z)}{\rho} dz, \tag{2.26}$$

Because of the orthogonality, the result is

$$\frac{1}{r}\frac{d}{dr}\left(r\frac{d\Phi_n}{dr}\right)+\sum_m 2B_{mn}\frac{d\Phi_m}{dr}+\sum_m A_{mn}\Phi_m+k*2_{rn}(r)\Phi_n=-\frac{\delta(r)\Psi_n(z_s)}{2\pi r}, \tag{2.27}$$

where

$$A_{mn}=\int\frac{1}{r}\frac{\partial}{\partial r}\left(r\frac{\partial\Psi_m}{\partial r}\right)\frac{\Psi_n}{\rho}dz, \tag{2.28}$$

$$B_{mn}=\int\frac{\partial\Psi_m}{\partial r}\frac{\Psi_n}{\rho}dz. \tag{2.29}$$

Equation 2.27 shows coupled modes in the environment of non-constant sound speed. The adiabatic approximation assumes that the coupling matrics A_{mn} and B_{mn} are negligible. Thus

$$\frac{1}{r}\frac{d}{dr}\left(r\frac{d\Phi_n}{dr}\right)+k_{rn}^2(r)\Phi_n=-\frac{\delta(r)\Psi_n(z_s)}{2\pi r} \tag{2.30}$$

To extend the 2-D model to a 3-D model, one can simply run the 2-D models repeatedly along a number of different bearings, i.e. an N × 2-D model where horizontal refraction has been ignored. The "Horizontal ray vertical modes" approach introduced in the next section is able to overcome this problem.[21]

2.3 Horizontal Refraction Equation

We return to the Helmholtz equation in three dimensions,

$$\rho\nabla\cdot\left(\frac{1}{\rho}\nabla p\right)+\frac{\omega^2}{c^2(x,y,z)}p=-\delta(x)\delta(y)\delta(z-z_s). \tag{2.31}$$

We seek a solution of the form of local mode $\Psi_m(x,y,z)$

$$p(x,y,z)=\sum_m\Phi_m(x,y)\Psi_m(x,y,z), \tag{2.32}$$

Substituting Eq.2.32 into Eq.2.31 and applying the operator

$$\int (\cdot) \frac{\Psi_n(x,y,z)}{\rho} dz, \tag{2.33}$$

yields

$$\begin{aligned} \frac{\partial^2 \Phi_n}{\partial x^2} &+ \frac{\partial^2 \Phi_n}{\partial y^2} + k_{rn}^2(x,y)\Phi_n + \sum_m A_{mn}\Phi_m \\ &+ \sum_m 2B_{mn}\frac{\partial \Phi_m}{\partial x} + \sum_m 2C_{mn}\frac{\partial \Phi_m}{\partial y} = -\delta(x)\delta(y)\Psi_n(z_s), \end{aligned} \tag{2.34}$$

where

$$\begin{aligned} A_{mn} &= \int \left(\frac{\partial^2}{\partial x^2} + \frac{\partial^2}{\partial y^2} \right) \Psi_m \frac{\Psi_n}{\rho} dz, \\ B_{mn} &= -B_{nm} = \int \frac{\partial \Psi_m}{\partial x} \frac{\Psi_n}{\rho} dz, \\ C_{mn} &= -C_{nm} = \int \frac{\partial \Psi_m}{\partial y} \frac{\Psi_n}{\rho} dz, \end{aligned} \tag{2.35}$$

assuming that the density $\rho(z)$ depends only on depth z. Neglecting the coupling matrices A, B and C, we have

$$\frac{\partial^2 \Phi_n}{\partial x^2} + \frac{\partial^2 \Phi_n}{\partial y^2} + k_{rn}^2(x,y)\Phi_n = -\Psi_n(z_s)\delta(x)\delta(y). \tag{2.36}$$

which can be solved by various 2D methods like normal modes, ray, or PE. In our study, we use ray model for its clear physics meaning.

2.4 Parabolic Equation Method

Start from the Helmholtz equation for a constant-density medium in cylindrical coordinates (r, φ, z) and for a harmonic point source of time dependence $exp(-i\omega t)$,

$$\frac{\partial^2 p}{\partial r^2} + \frac{1}{r}\frac{\partial p}{\partial r} + \frac{\partial^2 p}{\partial z^2} + k_0^2 n^2 p = 0 \tag{2.37}$$

where we have assumed azimuthal symmetry and it's independent on φ. Here $p(r,z)$ is the acoustic pressure, $k_0 = \omega/c_0$ is the reference wavenumber, and $n(r,z) = c_0/c(r,z)$ is the index of refraction. Assuming

$$p(r,z) = \Psi(r,z)H_0^{(1)}(k_0 r), \tag{2.38}$$

Substituting the trial solution, Eq. 2.38, into the Helmholtz equation, we obtain,

$$\frac{\partial^2\Psi}{\partial r^2} + \left(\frac{2}{H_0^{(1)}(k_0 r)}\frac{\partial H_0^{(1)}(k_0 r)}{\partial r} + \frac{1}{r}\right)\frac{\partial\Psi}{\partial r} + \frac{\partial^2\Psi}{\partial z^2} + k_0^2(n^2-1)\Psi = 0. \tag{2.39}$$

Using the far field assumption, $k_0 r \gg 1$, and Eq.2.20 we have

$$\frac{\partial^2\Psi}{\partial r^2} + 2ik_0\frac{\partial\Psi}{\partial r} + \frac{\partial^2\Psi}{\partial z^2} + k_0^2(n^2-1)\Psi = 0. \tag{2.40}$$

which can be solved numerically by Split-step Fourier transform method.

Chapter 3

SHALLOW WATER 2006 EXPERIMENT AND OCEANOGRAPHIC MEASUREMENT

In 2006, from mid-July to mid-September, a large, multi-disciplinary, multi-institution experiment named SW06 was conducted in the New Jersey coast. The SW06 experiment site is approximately 100 miles east of the New Jersey coast (Fig. 3.1), where internal waves are known to be generated during summer time. This site has been a research testbed for many previous experiments. To assess the relationship between the acoustic wave propagation and the internal waves, a total of 62 acoustic and oceanographic moorings were deployed with the geometry of a "T" to create an along-shelf path along the 80 m isobath and an across-shelf path starting at 600 m depth and going shoreward to a depth of 60 m.

A cluster of moorings was placed at the intersection of the two paths to create a dense sensor-populated area to measure 3-dimensional physical oceanography. Environmental moorings were deployed along both the along-shelf and across-shelf paths to measure the water column characteristics along those paths. Moorings with acoustic sources were placed at the outer ends of the "T" to transmit various signals along these paths. Five single hydrophone receivers (SHRU) were positioned on the across shelf path and a vertical and horizontal hydrophone array (VLA/HLA) was positioned close to the intersection of the "T" to have large antenna signal receptions from all the acoustics assets that were deployed during SW06.

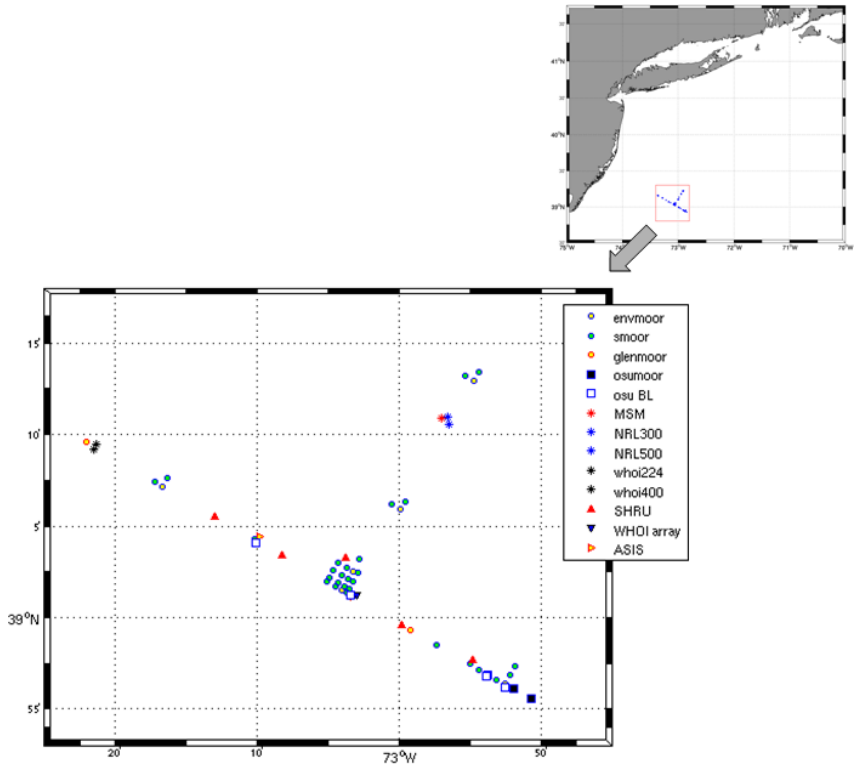

Figure 3.1: Map of SW06 experiment site and the locations of the environment and acoustic moorings

There were in total 34 environmental moorings deployed during SW06 experiment to monitor and record the physical oceanography of the area. Each of the acoustic moorings (source and receiver) was equipped with thermistors at various depths to help define the physical characteristics the acoustic channel. Close to the center of the "T" shape mooring layout, a thermistor farm consisting of 16 arrays were logarithmically spaced from 0.5 km to 3 km to record the internal waves at different scales.

Out of 34 environmental moorings, 6 of them were also equipped with an Acoustic Doppler Current Profiler(ADCP) to measure the current velocity at the location. The ADCP package including a temperature, conductivity,

pressure sensor was located about 7 m above the sea floor. The space of measuring bins was set at 1 m. The sampling interval of ADCP was 30 seconds and capable of resolving internal wave passage but not the fine scale of surface waves. Figure 3.2 shows the current data record by ADCP at mooring SW32 and the temperature data at the same location. It demonstrates the clear correspondence between the direction and the depth profile of the subsurface current.

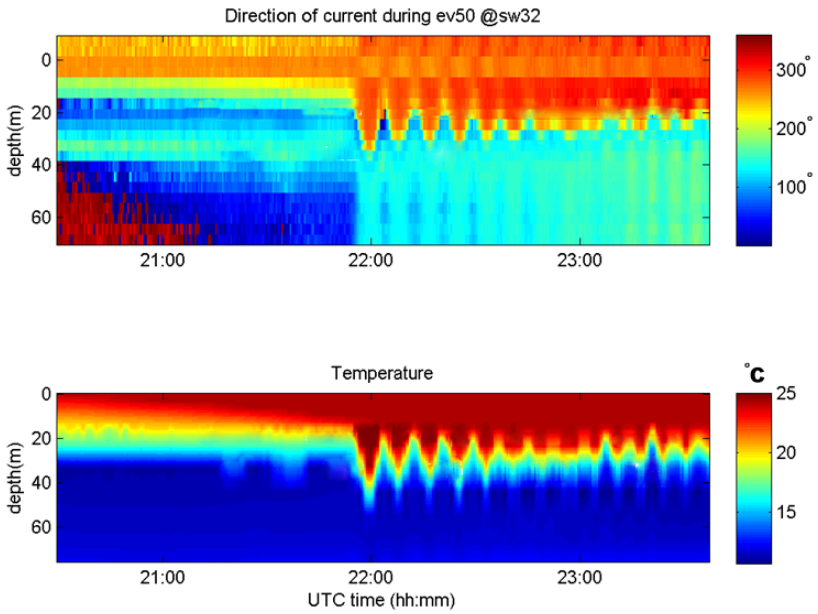

Figure 3.2: Current data record by ADCP at mooring SW32 on Aug.17, 2006(upper panel) and temperature data at the same location.

3.1 Internal Wave Observation

The SW06 site is known for generating internal waves. Figure 3.3 shows a radar image of the ocean taken by Canadian satellite RADASAT over the experimental site near the edge of the continental shelf. The picture shows about 10 groups of internal wave packets running diagonally from south-east to north-west, with the wave fronts approximately parallel to the edge of the continental shelf. The wave packets generated at the shelf break (about 200 m in depth) propagate towards the coast and dissipate at about 50 m. The separations between individual wave packets are approximately 10-20 km. Sever curvature is caused by the Hudson Canyon and numerous collisions between wave packets. Although bearing the word "internal" in its name, internal wave are visible to an electromagnetic radiation recording device such as a camera or a radar. Together with other factors like wind, surface waves, the subsurface current caused by internal waves changes the equilibrium surface and generates an alternating region of rougher or smother than average surface scattering of electromagnetic waves[4, 22]. The image captured by radar or optical device corresponds to the current under the surface. During SW06, two research vessels, R/V Oceanus from Woods Hole Oceanography Institution (WHOI) and R/V Sharp from the University of Delaware were constantly recording the surface expression of internal waves.

The passage of internal waves can also be seen by other environmental sensors. Figure 3.4 shows the depth of the 18^{o}C isotherm recorded on the WHOI VLA (SW54). Before the internal wave, the isotherm is at about 16 m, the first soliton wave pushs the isotherm down the 35m, and the later solitons even push further down towards the bottom. There are about 9 distinguishable soliton waves, followed by a long, slow-decreasing tail, the isotherm didn't

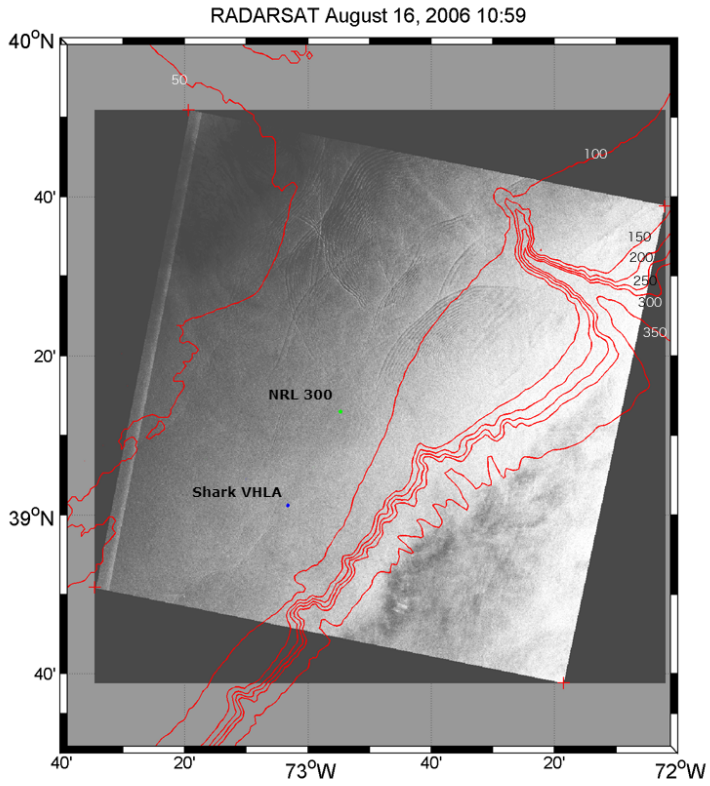

Figure 3.3: Image of SW06 experiment site taken by the Canadian RADARSAT satellite on 16 August, 2006. Bathymetric contours are overlaid and the positions of Shark VHLA and NRL300 sources are shown.

return to 16 m until 6:00 next day - the total duration of internal wave is about 8 hours.

Using the onboard radar of R/V Sharp of University of Delaware, 60 internal wave events were recorded when the surface expressions with various strength and direction were visible on the screen during the period of 21 days. Fig.3.5 shows their angular distribution. The directions spread from 280 to 330 degree with respect to north(0^o), with the strongest peak at about 320 degrees. The propagation paths and the speed vary considerably from one

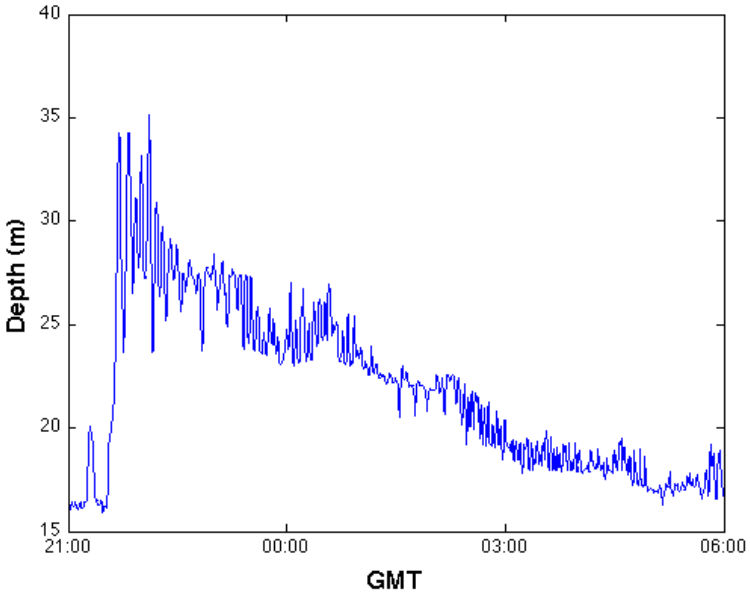

Figure 3.4: Depth of 18^oC degree isotherm on Aug. 17, 2006, recorded on WHOI Sharp VLA (SW54)

wave to another. Lynch *et al* [23] reported a similar results by studying satellite imagery. In this study, we focus on one internal wave event on August 17, 2006, when a complete set of acoustic and environmental data were collected simultaneously. In addition, the internal wave surface signatures were captured continuously by the on-board radars of two research vessels prior to the arrival of, and during the passing of, the internal wave packet over the acoustic track.

3.1.1 Internal Wave Event on Aug. 17th, 2006

On August 17, 2006, at about 18:00 GMT, the R/V Sharp from was located at $38^o59.262'$ N, $72^o57.492'$ W and the R/V Oceanus was located at $38^o57.426'$ N, $72^o56.676'$ W. Both platforms observed the origination of a internal wave packet near the shelf break.

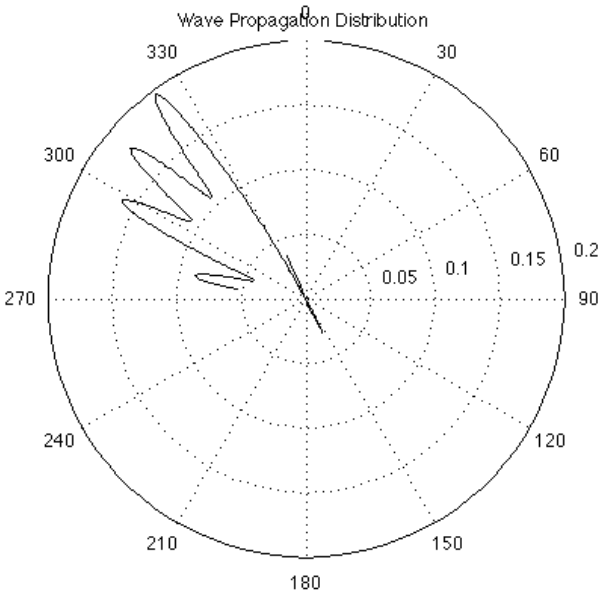

Figure 3.5: Angular distribution of the direction of the internal wave recored during SW06.

Figure 3.6 show the tracks of each vessel following this event from 18:00 GMT on August 17 to 02:00 GMT on August 18, 2006. The R/V Sharp's track was semi-circular, centered at the WHOI vertical and horizontal line array (Shark VHLA) with the ship being positioned on the trough of the leading internal wave front and moving with the advancing front. The R/V Oceanus followed the same internal wave packet from its initial location, while keeping a watch on the advancing wave front. Reversals in the track of R/V Oceanus indicate where the wave packet was crossed. During these periods, profiles of temperature, density, turbulence and sound velocity were measured. The two ships observed different parts of the internal wave front, which provided large spatial coverage. The surface signatures of the internal waves were digitally recorded by on-board ship radar every 30 seconds. Combined radar images

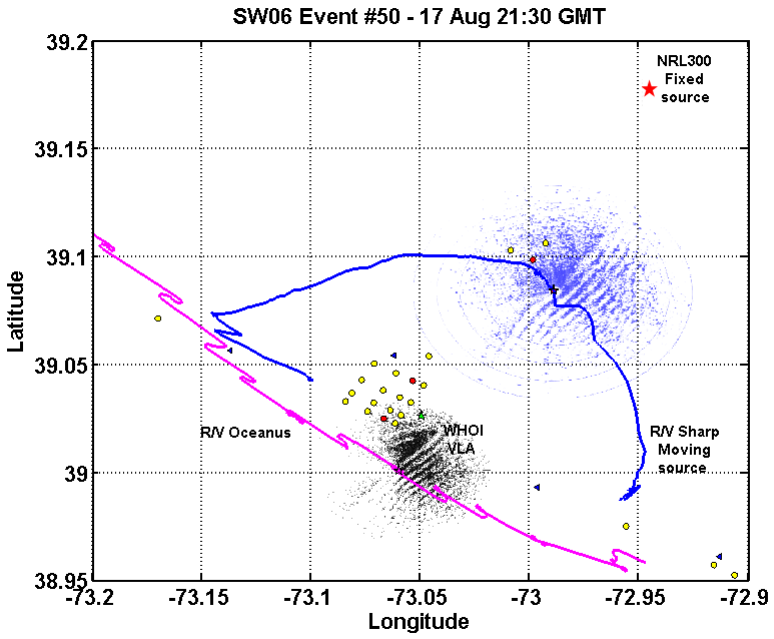

Figure 3.6: Diagram showing the fixed acoustic source(NRL300), receiver array (Shark VHLA) and the semi-circular track of R/V Sharp the IW on Aug. 17, 2006.

from the two vessels, each about 11.1 km in diameter, covered the receiver and about two thirds of the acoustic track.

3.1.2 Characteristics of the Internal Wave Packet

Since the internal waves are the dominant factor causing the fluctuation of the acoustic propagation, it is worthwhile to take a closer look at the characteristics of the internal wave packet. Temporally, the passage of the internal wave packets can be described by the speed and the direction of the wave train, which can be estimated either by averaging the direct measurement from the internal wave image captured by the ship radar, or by measuring the time difference when the leading front arrives at different thermistor arrays.

Table 3.1 lists the speed and direction estimations by these two methods.

Table 3.1: Direction and speed of the internal wave packet on Aug. 17, 2006.

Data source	IW speed	IW direction
Thermistor arrays	0.55m/s	325°
Ship radar	0.60m/s	330°

The vertical movement of the water column due to the internal waves, i.e., the vertical displacement of the isopycnal surfaces can be determined using temperature recordings. Temperature fluctuations are often regarded as proxies of the vertical displacement [24, 25], since the temperature effects are much more pronounced than salinity fluctuations. Ignoring the salinity fluctuation, the isopycnal surface is associated with the isotherm surface, therefore the time series of the vertical displacement of the isopycnal surface $\eta(t)$ can be deducted from the temperature recording by

$$T_i(z,t) = T_m(z_i) + \eta(t) \tag{3.1}$$

in which, z_i is the depth of the i-th thermistor, T_m is the mean temperature field before the internal waves, $T_i(z,t)$ is the temperature recording at the i-th thermistor. By moving the mean temperature field to match the instantaneous temperature recording, one can find the vertical displacement $\eta(t)$.

Figure 3.7 shows the vertical displacement at depth = 20, 30, 40 and 50 m below the surface (depth increase is positive in the downward direction) during the event. The depression is 15-20 m at different depths, and generally return to the mean level, with the maximum depression at depth=30 m, coincident with the location of the thermocline. The bottom half of the water (

below 50 m) didn't return to the mean temperature level, instead overshooting it, which indicates while in general internal waves carry warmer water, there can be a cold water current underneath the internal waves close to the bottom.

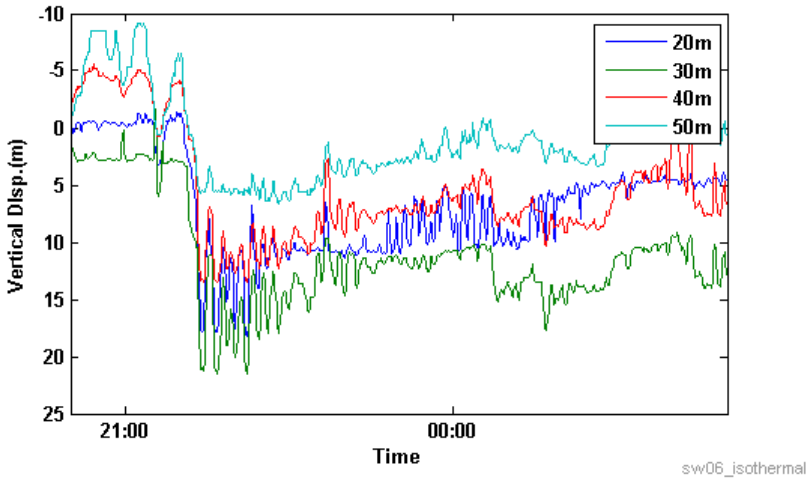

Figure 3.7: Time series of vertical displacement of internal wave at depth = 20, 30, 40 and 50 m, Aug. 7th - 8th. The depression is 15-20 m at different depths, and generally return to mean level. The greatest amplitude is measured at about 30 m, coincident with the location of the thermocline.

Figure 3.8 shows the high frequency oscillation of the vertical displacement time series by passing it through a high pass filter from 20 m to 50 m from the surface. The amplitudes of the high frequency oscillation generally decreases as the depth increases with the maximal amplitude (peak-to-peak) of 15 m at depth=30 m, which also has the greatest depression. The high frequency oscillation plot shows the period of the internal waves is about 5-6 min, together with the estimated internal wave speed in Table 3.1, the wavelength is about 150-200 m.

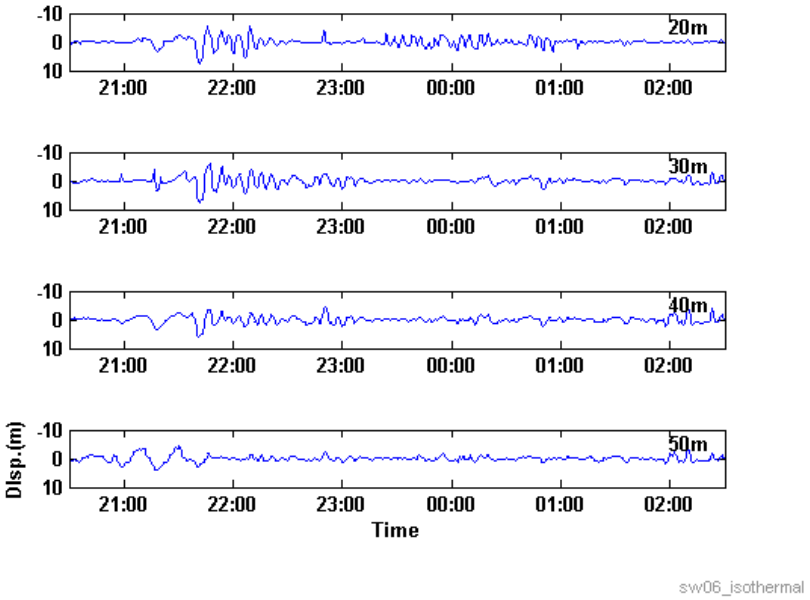

Figure 3.8: Time series of vertical displacement of internal wave (same measuring condition as in Fig.3.7 but filtered with a high-pass filter.

3.2 Acoustic Moorings

3.2.1 Underwater Acoustic Source

During SW06, several acoustic sources were used to transmit sound while environmental data were collected simultaneously [26]. Two Navy Research Lab (NRL) sources were deployed at mooring SW45 (the outer end of the along the shelf path). The 300 Hz source linearly swept over 270-330 Hz and the 500 Hz source linearly swept 470-530 Hz in 2.048 seconds every 4 seconds during their scheduled transmission cycle. Each also had a .2048 seconds (10% of transmission) amplitude taper (between 0 and 100% power) at the beginning and end of each transmission to allow for graceful ramping on and off.

The source was located 72 m below the sea surface and 10.5 m above

Table 3.2: Transmitted signals from fixed(NRL300) source

Source	Signal type	Frequency Band	Duration	Repeating rate
NRL300	LFM	270-330Hz	2.048sec	4sec
NRL500	LFM	470-530Hz	2.048sec	4sec

Table 3.3: Acoustic transmission during NIW event on Aug. 17, 2006

Transmission	Time(GMT)	Source
1	20:30-20:37	NRL300
2	21:00-21:07	NRL300
3	21:30-21:37	NRL300
4	22:00-22:07	NRL300
5	22:30-22:37	NRL300
6	23:00-23:07	NRL300
7	23:30-23:37	NRL300

the sea floor at $39^o10.957'$N, $72^o56.575'$W. Transmissions of Linear Frequency Modulated (LFM) signals from 270 to 330 Hz occured every 4 seconds. Transmissions continued for 7.5 minutes and then repeated every half hour.

Figure 3.6 shows the fixed source (NRL300), the receiver array (Shark VHLA) and the semi-circular track of R/V Sharp during the internal wave on Aug. 17, 2006.

Table 3.3 lists all the transmissions during the internal wave on Aug. 17, 2006 from fixed acoustic source

3.2.2 Underwater Acoustic Receiver Array

An "L" shaped vertical and horizontal receiver array (the "Shark VHLA") on mooring SW54 was located at $39^o01.252'$ N, $73^o02.983'$ W, about 20.2 km south of the NRL source. The vertical part ("VLA") of the receiver array

consisted of 16 hydrophones with 3.5 m spacing and was positioned in the water column from 13.5 m to 77.75 m below the surface. The horizontal part ("HLA") of the array consisted of 32 hydrophones on the seafloor with spacing of 15 m, providing 478 m of horizontal aperture. The sampling rate of the array was 9765.625 Hz. The water depth along the acoustic track was about 80 m.

3.3 Reconstruction of Three Dimensional NIW Environment

The water temperature data are collected by the thermistor string moorings at SW54 and SW32. Unfortunately, the surface sensor on SW32 was lost during the experiment, and the next one is located at 15 m down, thus some form of temperature extrapolation is necessary. Fifteen meter is the up bound of the fast-changing thermocline layer, which gives unrealistic results when using linear extrapolation. The water temperature can be as hot as $40°C$ at the surface. Help comes from a single pressure-temperature sensor attached to the transducer J15. On Aug. 17th and 18th, J15 were deployed and recovered twice, during which the TD sensor generated 4 temperature profiles shown in Fig. 3.9. The top layer of water is very well mixed, and the depth of it is about 13 m. The highest water temperature is about 25^oC. Based on this observation, the water temperature extrapolation/interpolation is performed for depth >15 m, for the water above 15 m, we assume the it is well mixed, which justifies the use of the temperature measured at the top sensor (15 m).

A detailed, accurate 3D environment is critical in order to model the acoustic propagation in the area, and for a better understanding of the acoustical phenomena occurred during the experiment. However, limited by the equipment and experiment conditions, environmental data usually can only

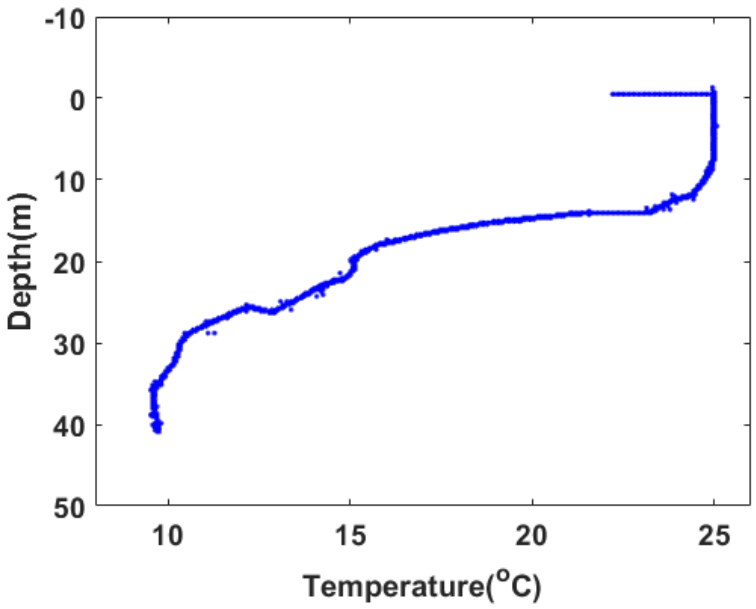

Figure 3.9: Depth-temperature plot from J15 temperature sensor data collected from 23:22:50-23:31:00, June 22. Data shows for the first 13m, the sea water is well mixed and the temperature is constant $\sim 25^oC$.

be gathered at sparse mooring points (relative to the large scale of water body). Next, we explain how we reconstruct the 3D temperature field from various sources and sensors for NIW during the SW06 experiment.

Figure 3.10 shows the combined radar picture of IW at 22:00GMT from R/V Oceanus and R/V Sharp with sketched leading wave fronts (red dash line). While the internal wave fronts in general remain relatively straight across the range (10km), it does demonstrate some curved features under close examination. It's also worth noting that within the range of R/V Oceanus's radar (lower one), and the upper half of R/V Sharp's radar, the wave fronts are indeed pretty straight, which leads us to believe a 3-segmented line could be a better approximation for a more accurate model without too much manual

sketch. Under this assumption, the interpolation on the x-y plane is done on the direction parallel to the IW fronts, i.e., perpendicular to the direction of wave propagation.

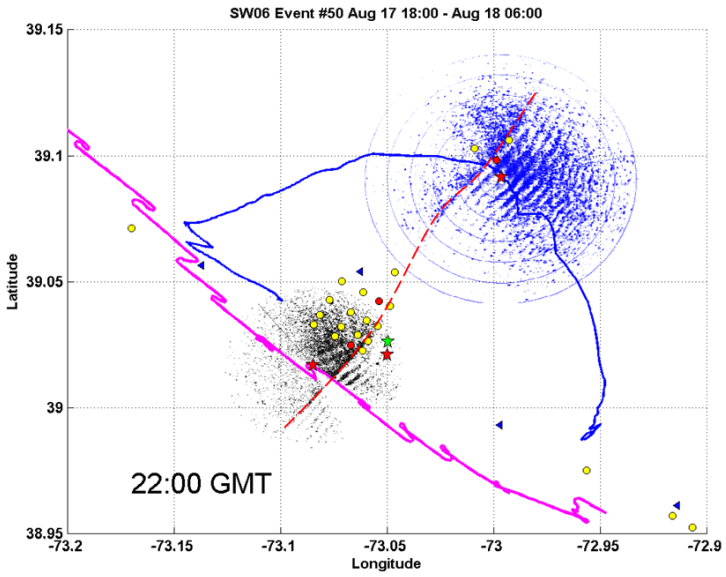

Figure 3.10: Combined radar images from R/V Sharp(blue) and R/V Oceanus(black). Blue and pink lines show their ship tracks during the internal wave event on Aug. 17, 2006. A red dashed line outlines one possible shape of the leading fronts.

The speed and direction of the leading IW front are estimated from temperature sensor data as well as the measurements from radar images. Speed and direction are optimized with the MMSE (minimum mean square error) criteria. Consider the size of the T-farm, it is not as "local" as the other two estimations. Nevertheless, all three estimations show very similar results, and again confirmed by the radar observations. The consistence implies when the IW is passing the Shark-SW32 acoustic track, the wave packet as a whole is stable in terms of both shape and moving velocity.

Table 3.4: Local velocity and direction of the internal wave packet on Aug. 17, 2006.

Location	Moorings	IW front direction	IW speed (m/min)
Shark VLA	54,14,15,16,17	38.3022	55.6164
T-farm	4-17, 30, 31	36.8208	53.6021
Madway	32,19,20	39.5210	57.6753
R/V Sharp Radar		$\sim$40	57.5653
R/V Oceanus Radar		$\sim$40	55.1065

Based on the estimated IW speed and direction, we can reconstruct a 3D temperature field. Figure 3.11 shows the reconstructed temperature field at 15 m. The reconstructed temperature field matches well with the curved leading internal wave front recorded by two ship radars, as well as the trailing 8 waves. The mean estimated IW speed (54.4293 m/min) and direction (51.0884 degree w.r.t. North) were used.

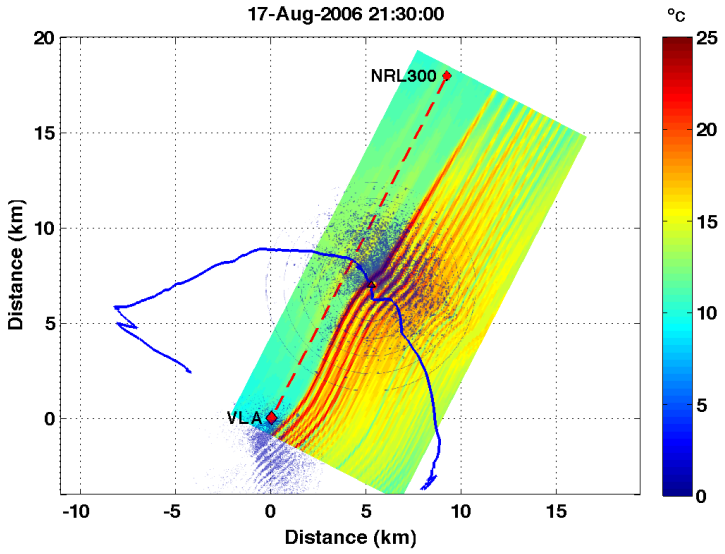

Figure 3.11: Reconstructed environment at 21:30:00, Aug. 17th (Depth = 15m). The temperature matches well with the curved internal wave fronts from two radar images.

Chapter 4

ACOUSTIC OBSERVATION AND MODELING IN THE INTERNAL WAVE EVENT

Our goal in SW06 experiment is to examine the relationship between internal waves and acoustic wave propagation. In particular, we seek to understand the acoustic wave propagation mechanisms governed by the direction of the acoustic track relation to the internal wave front.

The propagation of acoustic signals is strongly related to the ocean's physical attributes with various time scales and frequencies, such as surface waves, internal waves, tides, currents. Given the conditions of SW06 experiment (acoustic signal transmission interval = 4sec, acoustic listening window = 3hr), we concentrated ourselves to the variation caused by the internal wave activities.

While there are multiple acoustic sources deployed in SW06 experiment, we will focus on the chirp signal transmitted made from NRL300 source. Matched filtering technique is used to compress the signal and increase the signal to noise ratio(SNR) before further processing. Matched filter technique can be expressed as

$$y[n] = \sum_{k=-\infty}^{+\infty} s[n-k]x[k] \tag{4.1}$$

in which, $x[k]$ is the received signal as a series of time, $s[k]$ is the transmitted signal and $y[n]$ is the matched filter output. Figure 4.1 shows a chirp signal received at GMT15:57:04, Aug 03rd, before (a) and after (b) matched filter.

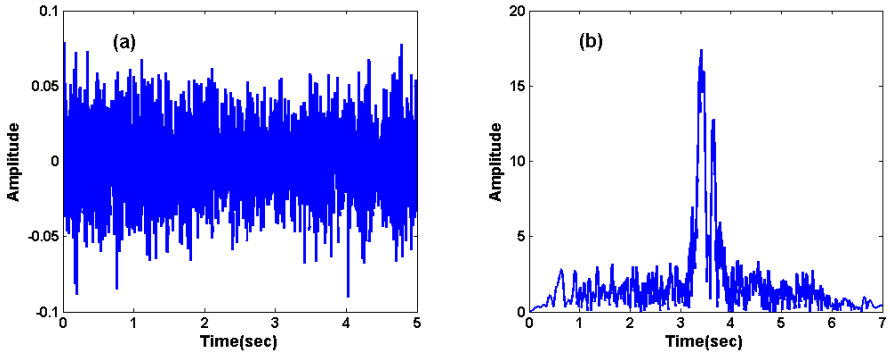

Figure 4.1: Received chirp signal on Shark array at GMT15:57:04, Aug 03rd, (a)before and (b)after matched filtering.

4.1 Acoustic Transmission Received on Shark Array

Figure 4.2 shows the geometry of the source(B) and receiver array(A) and the approaching NIW solitons, with one extra environment mooring to help collect temperature data. Distances from A, B and C to the leading NIW front are estimated from the reconstructed environment and summaries in Table 4.1 summaries the time of transmission and distance from A, B and C to the leading NIW front.

All three moorings were equipped with thermistor strings and continuously took temperature measurement during the event. Left column of Fig.4.3 shows the temperature profiles measured at these moorings. The progress of NIW is clearly shown in Fig.4.3, when the leading front arrived at the source(B), middle(C) and receiver(A) at 22:15, 22:00 and 21:45 respectively. Right column shows the sound speed profiles(SSP) calculated from the temperature data taken at the beginning of each transmission. The movement of the SSPs indicates the dynamic behavior of the thermocline.

Table 4.1: Summary of transmission schedule during geotimes Tg_1 to Tg_4 listing the distance between the NIW front to the acoustic track. (Distances are in km. Positive distance indicates the leading NIW front is at the south-east side of the acoustic track, negative distance indicates the front is at the north-west side of the acoustic track)

Geotime	Start	End	d1(km)	d2(km)	d3(km)
Tg_1	21:00	21:07	2	4	5
Tg_2	21:30	21:37	0.5	1.5	2
Tg_3	22:00	22:07	-1	0	1
Tg_4	22:30	22:37	-3.5	-2	-1

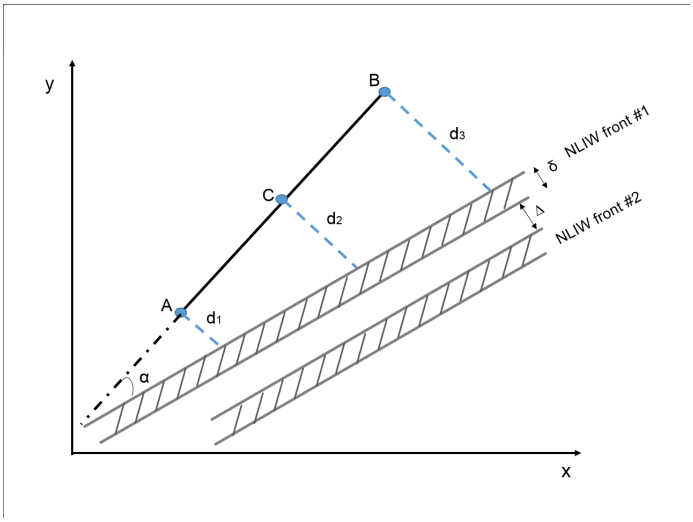

Figure 4.2: Schematic diagram showing the geometry of the fixed sound source (point B) and receiver array (point A) and the NIW soliton approaching at angle of α between its straight line wave front and acoustic track AB. Mooring SW32 (point C) was located at the midle to provide additional temperature measurement.

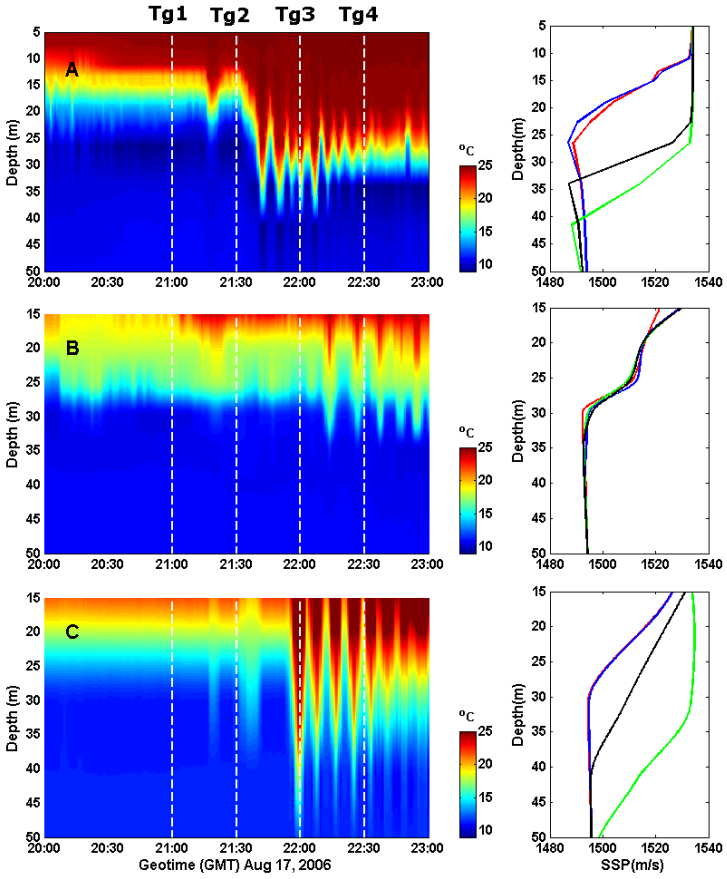

Figure 4.3: Temperature profiles measured at (A) the acoustic source, (B) at the shark VLA array, and (C) the midpoint between the source and receiver during August 17, 2006 from 20.00 to 23:00 GMT. The geotime intervals Tg_1 through Tg_4 are tabulated in Table 4.1. For the shallow water region, with small changes to the salinity profile, we consider the temperature profile to be representing the behavior of the sound speed profile (SSP). For each sub plot, the SSP profiles for the four geotimes are shown on the right panel indicating the dynamic behavior of the thermocline.

4.1.1 Transmission 21:00-21:07GMT

This the quiescent phase before the internal wave packet arrive at the source-receiver track and have little impact on the acoustic propagation. Figure 4.4(a) shows the reconstructed temperature field at the beginning of the transmissions (21:30GMT). The same field will be used as the environmental input for acoustic modeling in the later section. The overlay consist of scattered blue dots is composed from the captured sea surface radar images on R/V Sharp and R/V Oceanus, enhanced by image processing tools. The radar overlay shows the curved internal wave fronts with one extrusion centered at the track of R/V Sharp (blue line), and the other one half located south-west outside of the interpolated field. Three moorings are marked on the plot, (A) Shark receiver array, (B) NRL300 source and (C) middle point mooring.

Figure 4.4 shows the received signals (squared matched filter output) on Shark array for the transmission from 21:00 through 21:07GMT. Panel (b) Panel (b) shows the geotime-frequency spectrogram of the received signal. The energy is concentrated at the center frequency(300Hz) but shows little variation in time. Panel (c) plots the received signal on the vertical leg of the Shark array (VLA). It shows a three stripes at depth of 22, 30 and 70m, approximately. Overall, the 3-strip pattern is very stable, with a slight dip on the bottom stripe at the middle. The blue line shows the depth-integrated intensity during the transmission, with a peak-to-peak amplitude about 5dB. Notice the frequency is about 0.1 Cycle/minuet (cpm). This is a magnitude different with the fluctuation caused by the internal wave shown in Fig.4.5,4.7 and 4.8, which generally at <1 cpm range. Acoustic intensity of mode 1-6 is shown in panel(d). Mode 1-4 are the dominant modes with mode 3 being

the strongest. Most modes are stable during the transmission except mode 5 shows a increase in intensity at arrival time of 0.4sec. This observation is consistent with panel (b) and (c).

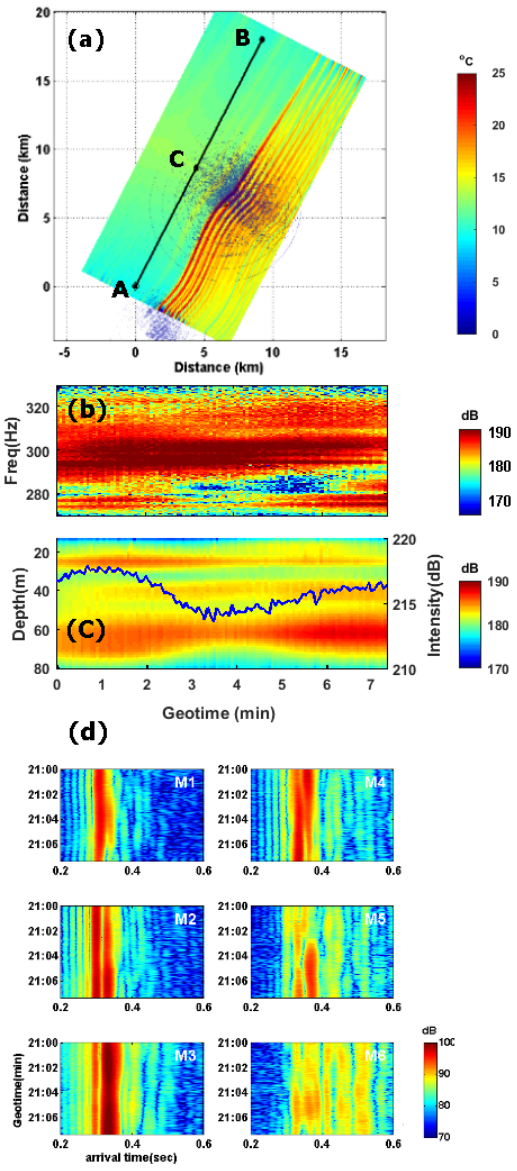

Figure 4.4: Positions of the acoustic receiver (A), source (B), and a thermistor chain in the mid-point (C) at Tg_1 (21:00 GMT). (b) Geotime-Frequency spectrogram showing the received signal from 21:00 to 21:07 GMT. (C) Signal intensity versus geotime in depth. Blue line is the depth integrated intensity. (d) First six modes filtered using modal decomposition.

4.1.2 Transmission 21:30-21:37GMT

This phase of particular interests here because from the internal wave map (Fig. 4.5(a)), the leading front of the IW packet is still at about 1km away from the Shark VLA at the end of the transmission session (21:37GMT), yet its impact on the acoustic propagation started to be seen on the received signal on the Shark array. The received signal spectrogram and intensity on Shark array (Fig.4.5(b) and (c)) all show a clear contrast between the first and second halves of this transmission. During the first half, the signal continues the steady characteristic from phase I. When the IW moves closer in the second half, the acoustic signal changes to a oscillating two-strip pattern. On the other hand, the depth-integrated intensity shows a small fluctuation ($< 4dB$), which implies the energy at the vertical plane is more or less conserved, the changing is mainly due to some horizontal disturbance. There are 10 sloped stripes shown in the spectrogram, which will be further analyzed in the next section.

As the modal decomposition plots shown in Fig.4.5(d), all 6 modes were affected by the approaching internal waves with the second half showing oscillating patterns. Majority of acoustic energy is contained in the lower modes (mode 1-4), with mode 3 and 4 being the strongest. Meanwhile, mode 3 - 6 all have a later arrival appeared around half way through the transmission and converged close to the end. This is no coincident that the later arrivals come almost the same time with the oscillating patterns but the direct evidence of horizontal Lloyd's mirror effect.

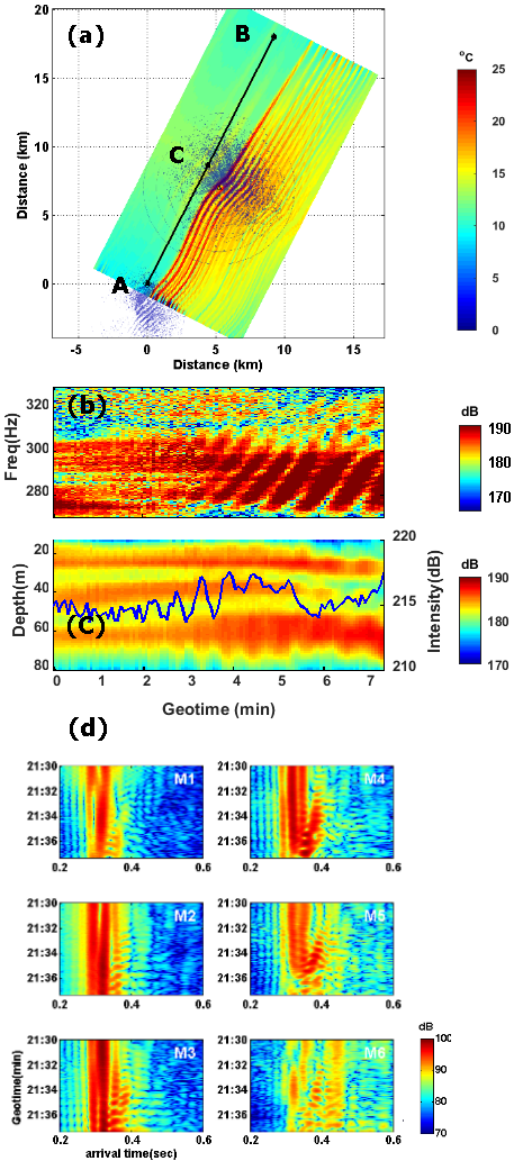

Figure 4.5: Positions of the acoustic receiver (A), source (B), and a thermistor chain in the mid-point (C) at Tg_2 (21:30 GMT). (b) Geotime-Frequency spectrogram showing the received signal from 21:30 to 21:37 GMT. (C) Signal intensity versus geotime in depth. Blue line is the depth integrated intensity. (d) First six modes filtered using modal decomposition.

4.1.3 Transmission 22:00-22:07GMT

In this phase, the acoustic signal propagates through the body of the IW packets. Previous research shows[27, 28], that the position of the source and receiver in internal waves can cause fluctuations ($> 6dB$) in the received signal by mechanisms like refraction, focusing and defocusing depending on the relative positions of the source and receiver in the internal waves. At 22:00GMT, the source is about three kilometers from the leading wave front, but the Shark VlA is at the trough between the second and the third waves, and about half of the acoustic track is directly interacting with the IW packet (Fig.4.7(a)). The internal wave packets occupies the most of the acoustic path.

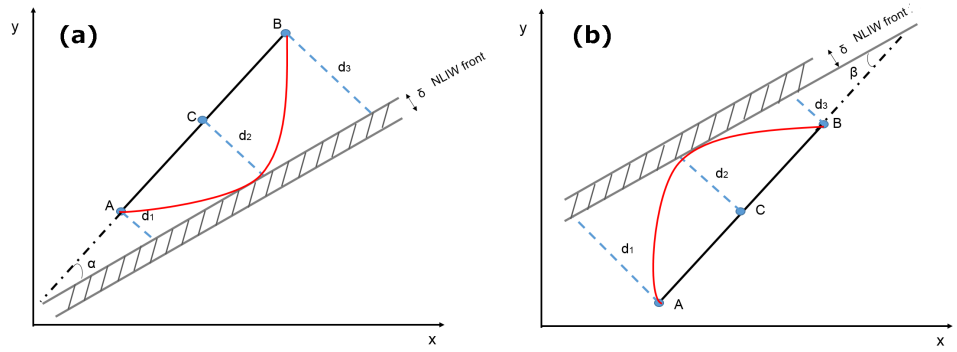

Figure 4.6: (a) The position of the NIW soliton front before it arrives at acoustic track AB. (b) The position of the NIW soliton front before it arrives at acoustic track AB.

The spectrogram shows a similar pattern of strips as previous transmission but with reversed. On the VLA (Fig.4.7(b)), the three-stripe patterns

seens in the previous transmissions have been replaced with a broken two-stripe one. At around 5min after the beginning of the transmission, there is a great increase of acoustic intensity followed by a deep decrease. The integrated intensity fluctuation is as great as 15dB. This is consistent with the impact of horizontal focusing/defocusing mechanisms. Rather than redistributing the energy within the vertical plane, the acoustic energy is converging from the horizontal vicinity.

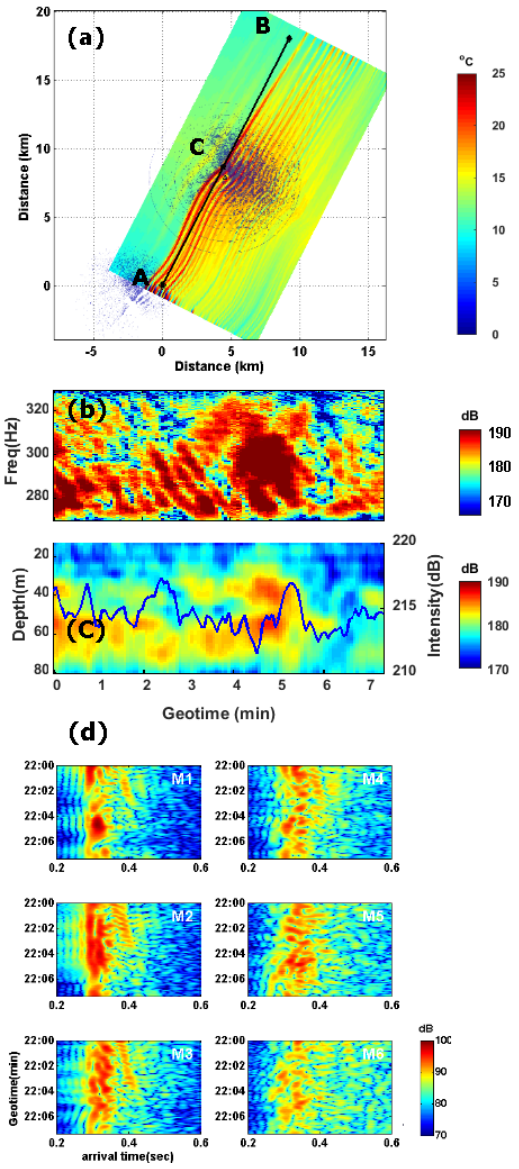

Figure 4.7: Positions of the acoustic receiver (A), source (B), and a thermistor chain in the mid-point (C) at Tg_3 (22:00 GMT). (b) Geotime-Frequency spectrogram showing the received signal from 22:00 to 22:07 GMT. (C) Signal intensity versus geotime in depth. Blue line is the depth integrated intensity. (d) First six modes filtered using modal decomposition.

Modal decomposition (panel d) shows the acoustic energy has been transferred from mode 3 and 4 to mode 1 and 2, while the higher modes (5 and 6) remain weak. This explains the 2-stripe pattern in the geotime-depth intensity plot (panel c). At 5min mark, mode 1, and to a less degree, mode 2 are the dominant play of the focusing mechanism with a sudden increase in amplitude. On mode 1-4, there is a later arrival from 0.35sec to 0.45sec. This time, the later arrival has the reverse behavior of the one in the previous transmission: it is closer to the main arrival the the beginning of the transmission, but diverges as the transmission continues, and dissipates around 22:04GMT. This is another demonstration of Lloyd's mirror effect, but with leaving internal wave fronts.

Figure 4.6 shows the positions of the NIW soliton front before it arrives at the acoustic track AB (panel a) and when it's leaving the acoustic track (panel b), corresponding to transmission 21:30-21:37 and 22:00-22:07.

4.1.4 Transmission 22:30-22:37GMT

At 22:30GMT, the first 6 strong internal wave fronts has left the Shark array while the source is still in the crest of the second front of weakened internal wave packets (Fig.4.8(a)). The spectrogram (panel b) shows the energy is concentrated at the lower half of the frequency band (270-300Hz). There are two sloped strips but with much longer interval compared to the stripes caused by Lloyd mirror effect in previous transmissions. The received signal intensity (panel c) does not show a striped pattern, but instead a patched image. After 2 minutes, one focusing event of $> 5dB$ intensity increase happens at around 2-4min mark, with the acoustic energy concentrated at the water column from 20m to 40m, followed by a steep decrease. The sudden change of the depth-integrated intensity implies out-of-plane energy concentration and

spreading, confirming a focusing/defocusing event. On the contrary, the energy transfer from 40m to 60m (5min to 7min mark) shows little fluctuation on the depth-integrated intensity plot, which suggests a in-plane energy transfer, and can be tentatively explained by the warm water depression often follows the internal wave packets.

The modal decomposition results are shown in panel d. It is clear that, at the beginning of this transmission, all six modes are very weak until the onset of the focusing event, which selectively increases the intensity of mode 1,4 and 5, and mode 1 since becomes the dominant mode, with mode 4 and 5 drop out when the focusing area leaves the receiver, and the "shadow" zone moves in.

In this section, we documented the effects of the passage of a NIW packet on the acoustic propagation from before, during and after the fronts arrive at the acoustic track. In the next section, we will take a close look at the data and use numerical models to explain the mechanisms that cause them.

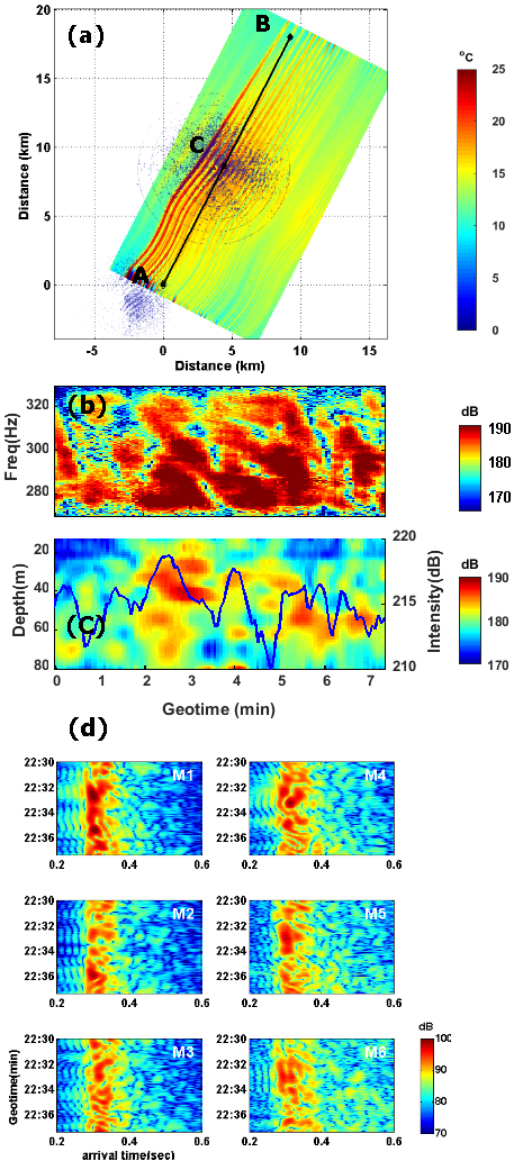

Figure 4.8: Positions of the acoustic receiver (A), source (B), and a thermistor chain in the mid-point (C) at Tg_4 (22:30 GMT). (b) Geotime-Frequency spectrogram showing the received signal from 22:30 to 22:37 GMT. (C) Signal intensity versus geotime in depth. Blue line is the depth integrated intensity. (d) First six modes filtered using modal decomposition.

4.2 Horizontal Lloyd's Mirror Effect

There are multiple occurrences in the SW06 experiment when geotime-frequency striations were discovered in the spectrogram of acoustic intensity $I(T_g, \omega) = |p(T_g, \omega)|^2$, where T_g is the geotime and ω is the acoustic frequency. Fig 4.9 shows the similar phenomena occurred at three different times. The most prominent one happened in the event 50 on Aug 17th, and it is the focus of this study.

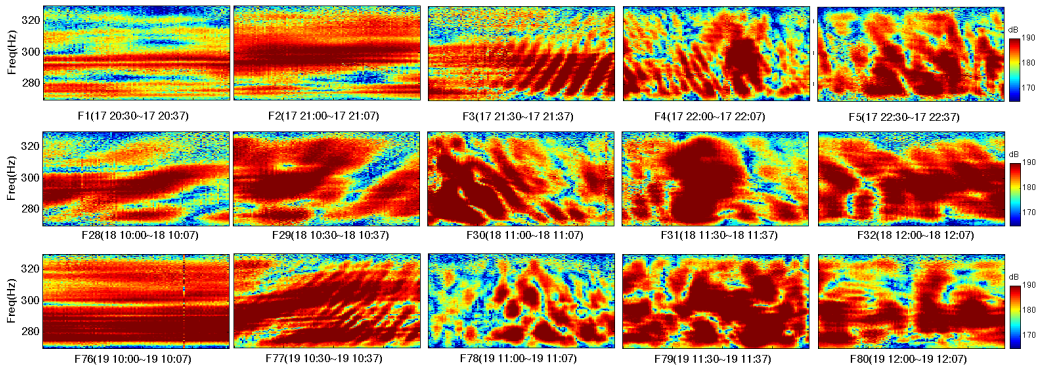

Figure 4.9: Geotime-frequency striations at different time during SW06 experiment at GMT20:30-22:37,Aug 17th(top row), GMT10:00-12:07, Aug 18th(middle row) and GMT10:00-12:07, Aug 19th(bottom row).

In previous studies[29, 30], the striations discussed are generally frequency-range striation and caused by the movement of the source, whereas the ones observed in SW06 were induced by the movement of the internal wave packet, especially the leading fronts. And when the explanations for the aforementioned studies rely on the intermodal interferences, the dominant mechanism

cause here is the combination of intermodal and inter-path interferences.

4.2.1 Two-Dimensional Model

We start with 2D propagation case on the horizontal plane in an environment with an approaching wave front. This provides a concise picture of the relationship between the internal wave movement and the acoustic propagation.

Figure 4.10(a) and 4.10(b) show the temperature data recorded on the thermistor array collocated with NRL300 source and the Shark VLA. The start and end times of the 7.5min transmission session are marked by two dashed lines. The leading front of the internal wave arrived at the receiver at 21:40GMT, and at 22:20GMT at the source. At the same time, the surface expressions of the internal waves were recorded by two ship-born radars as the R/V Sharp from the University of Delaware and as the R/V Oceanus from WHOI. Using the temperature data and radar images, the speed of the internal wave is estimated at 0.8m/s, and the angle between the acoustic track and the internal wave front is estimated as 5o. The intensity of received LFM signals coherently averaged over the array in one 7.5min transmission session (21:30-21:37GMT) is plotted in Fig. 4.10(c). From 21:33GMT, its spectrogram in Fig. 4.10(d) shows a strong time-frequency pattern of inclined stripes. The energy is more concentrated in the lower half of the signal frequency band (270-300Hz). As the internal wave moves closer to the receiver, the stripes become broadened. In Fig. 4.10(d), seven stripes depicting the spectrogram minima are identified. Measured at a frequency of 285Hz, the intervals between two adjacent lines are 34, 39, 42, 43, 44 and 46, all in seconds. The slope of the stripes is about 40Hz/min.

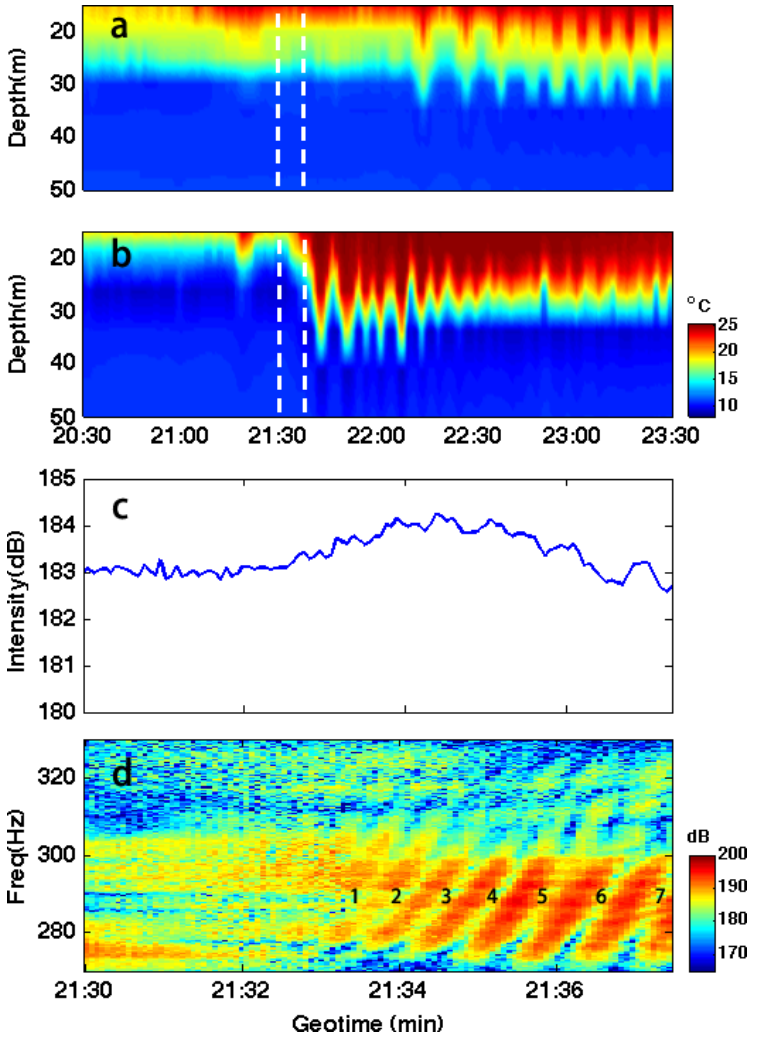

Figure 4.10: Temperature data recorded on (a) the acoustic source and (b) on the Shark VLA receiver from 20:30 to 23:30GMT, on Aug 17th, 2006. The start and end time of the transmission session are marked by two dashed lines. (c) Depth-averaged intensity of received LFM chirps on the Shark VLA hydrophone array during the transmission session from 21:30 to 21:37GMT. (d) Averaged spectrogram of received LFM signal.

We assume the high temperature front brought by internal waves is well mixed and across the entire water column. This assumption effectively reduces the problem to a 2D case. Figure 4.11 shows the geometry of the simplified experimental setup on the horizontal plane. For a single frequency acoustic signal, the acoustic pressure at receiver can be written as

$$p(r,t) = a_1 e^{i(\omega t - k_{r1})} + a_2 e^{i(\omega t - k_{r2})} \tag{4.2}$$

r_1 is the direct path between the source and receiver, and r_2 is the reflected (or refracted) ray path from the high temperature internal wave front in horizontal plane, hense a function of geotime $r_2 = r_2(T)$. Here, a_1 and a_2 are the amplitudes of acoustic wave along two paths. ω is the angular frequency, k is the acoustic wavenumber, and as usual, $k = \frac{\omega}{c}$, where c is the sound speed.

The intensity of a single frequency acoustic signal $I = |p|^2$ is,

$$I(T) = a_1^2 + a_2^2 + 2a_1 a_2 cos\{k[r_1 - r_2(T)]\} \tag{4.3}$$

Figure 4.12(a) shows the intensity as a function of both geotime and frequency using the internal wave speed estimated from SW06 data. The interference pattern produced by Eq.4.3 is very similar to the one observed in the experiment data, which in turn justifies the merit of the two-layer assumption. The direction of the stripes depends on whether the internal wave is approaching or leaving the acoustic track.

The integrated acoustic intensity of a LFM signal can be written as:

$$I_{int} = (a_1^2 + a_2^2)\Delta\omega + \frac{4a_1 r_2 c}{r_1 - r_2}\left(sin\frac{\Delta k(r_1 - r_2)}{2} \cdot cos(k_c(r_1 - r_2))\right) \tag{4.4}$$

in which $\Delta\omega = \omega_2 - \omega_1$ is the bandwidth of LFM signal, $\Delta k = k_2 - k_1$ and k_c is the wavenumber of the center frequency. The first part in Eq.4.4, $(a_1^2 + a_2^2)\Delta\omega$ represents the mean intensity of the acoustic signal, and the

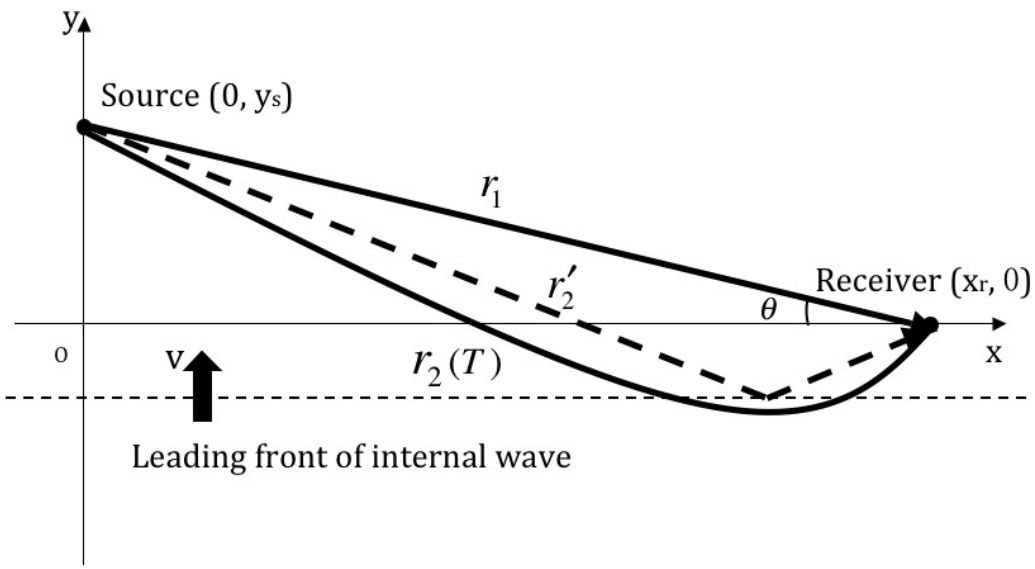

Figure 4.11: Diagram of source-receiver track relative to the leading internal wave front moving at speed = v. r_1 is the direct path, r_2 is the refracted path, and r_2' is reflected path under the two-layer assumption.

second part indicates the broadband LFM signal oscillations at same period as a monotone signal at the center frequency [compared to Eq.4.3]. While the mean intensity keeps the same, as the internal wave approaches the acoustic path, the envelope of the signal increases at the rate of $4a_1a_2c/(r_1 - r_2)$ and its amplitude increases rapidly [Fig.4.12(b)].

The period Γ and the slope of the beating interference patterns shown in Fig. 4.10(d) both increase as the internal wave front approaches the acoustic track. Although the slope only changes slightly during the 7.5min transmission time, it is a measurable quantity that can be calculated as follows. From Eq. 4.3, the angular frequency of the oscillating intensity $I(T)$ as a function of wavenumber k is

$$\Omega = \frac{d}{dt} k(r_1 - r_2) \tag{4.5}$$

If specular reflection assumption is used (i.e., the path shown by the dashed line in Fig. 4.11), Ω can be written as a function of the IW approaching speed v, the source position $(0, y_s)$ and receiver position $(x_r, 0)$.

$$\Omega(T) = 2k \frac{(y_s - 2vT)v}{\sqrt{x_r^2 + (y_s - 2vT)^2}} \tag{4.6}$$

The period of the beating oscillations is simply $\Gamma(T) = 2\pi/\Omega$, and is a function of the geotime. As the IW front gets closer to the acoustic path, interference between the direct and reflected (or refracted) paths causes a beating pattern. Using the specular reflection assumption, we can write the period as

$$T = \frac{\pi\sqrt{x_r^2 + (y_s - 2vT)^2}}{k(y_s - 2vT)v} \tag{4.7}$$

The minima of the acoustic intensity are at $\cos k(r_1 - r_2) = -1$, which give the difference of the two paths as

$$r_1 - r_2 = (2n + 1)\pi/k \tag{4.8}$$

in which, the integer n represents the order of stripes. The acoustic frequency $f = kc/2\pi$ can be written as a function of geotime through r_2 as

$$f = \frac{(2n+1)c}{2(r_1 - r_2(T))} \tag{4.9}$$

The slope $s = df/dt$ of the n-th stripe in the time-frequency spectrogram is

$$s = \frac{d}{dT}\left(\frac{(2n+1)c}{2(r_1 - r_2(T))}\right) \tag{4.10}$$

Using specular reflection assumption,

$$s = -c \cdot v(2n+1)\frac{(y_r + y_s - 2vT)}{(r_1 - r_2)^2 r_2} \tag{4.11}$$

Figure 4.12(c) shows the period and the slope for the same time duration as in Fig. 4.12(a) and 4.12(b). As the internal wave front moves closer to the receiver, the period increases, which corresponds to broader stripes in the interference pattern, as shown in Fig. 4.10(c).

4.2.2 Three-Dimensional Model

As described in chapter 2, two types of 3D acoustic models, parabolic equation model and vertical-mode horizontal-ray model, are used to simulate the impacts on acoustic propagation due to the passing of internal wave packets, particularly the interferencs due to the horizontal refracted/reflected acoustic signals, i.e., the horizontal Lloyd's mirror effect.

Figure 4.13 shows the horizontal ray plot of vertical mode 1-3 in a simplified environment of transmission 3, when the leading wave front just passes position R, the vertical line array anchor position. All modal rays of three modes are bent by the internal wave front, but with different severity. The first mode shows some degree of ray bending, around the internal wave fronts.

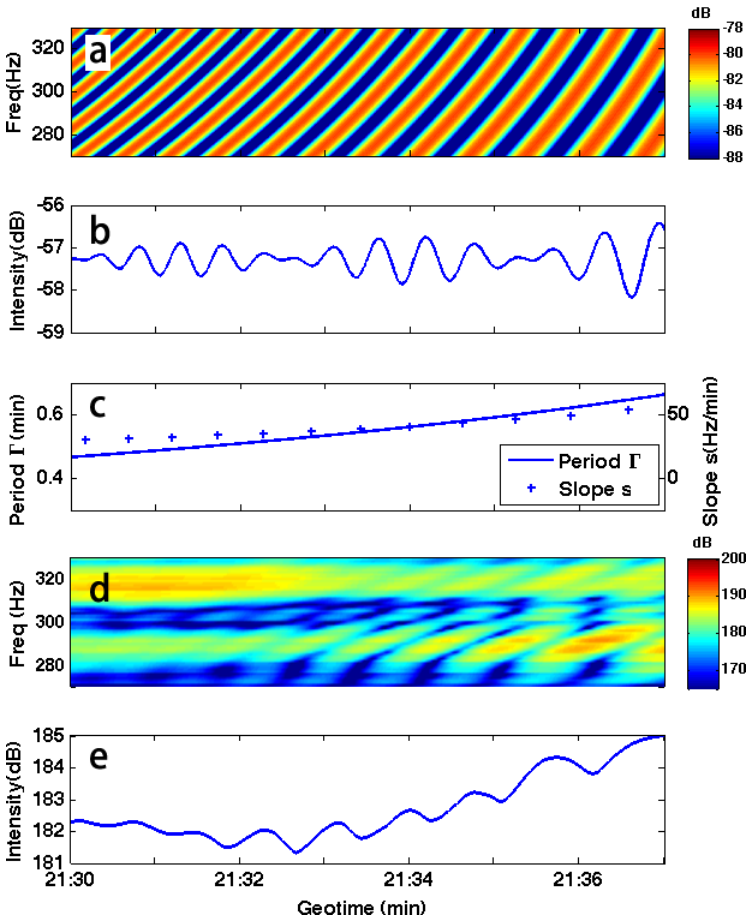

Figure 4.12: Simulated acoustic spectrogram and intensity as a function of geotime. (a) Spectrogram using two-layer assumption [Eq.4.3]. (b) Intensity of a broadband LFM signal (270-330Hz) using two-layer assumption [Eq.4.4]; (c) Period and slope of the interference pattern [Eq.4.7 and 4.11]. (d) Spectrogram from 3D PE model. (e) Intensity of a broadband LFM signal (270-330Hz) from 3D PE model.

However, refraction can barely be observed at the horizontal line array, which is not yet covered by the incoming internal waves. The second mode shows stronger refraction around the internal wave front and minimum refraction at the horizontal line array. Compared with the first two modes, the third mode shows drastic effects of the refraction. A large portion of the rays reflects off the leading internal waves. Only a small portion of the third mode rays penetrate and refract between the two edges of the internal waves. Additional third mode rays appear at the horizontal line array, due to the strong refraction and reflection induced by the internal waves. Multiple refracted and reflected rays indicate possible interference among them.

The second column of Fig.3 shows the arrival time fluctuations for the first three modes, observed at position R, when the internal waves pass through the acoustic track. The three rows show the results for the three modes, respectively. In each of the subplots, the horizontal axis represents the relative arrival time in milliseconds. The vertical axis shows the geotime in minutes, during which the internal waves pass through the region. Overall, the modal arrival time fluctuations show strong variation across the modes due to the horizontal refraction of the sound field. In the simulation, the first mode shows small arrival time fluctuations in several milliseconds. The second and third modes show much larger fluctuations, up to 50 ms for the third mode. In addition, at position R, multiple returns are simulated for all the three modes. However, only the second and third modes have significant separation, in tens of milliseconds.

We can also using Parabolic Equation model to simulation the propagation of a single mode. In Fig.4.14,the depth-integrated intensity of vertical modes 1, 2 and 3 are plotted. The simulation environment has two internal waves at about $y_1 = -1.0 \sim -0.5km, y_2 = 0.1 \sim 0.5km$ positions and the

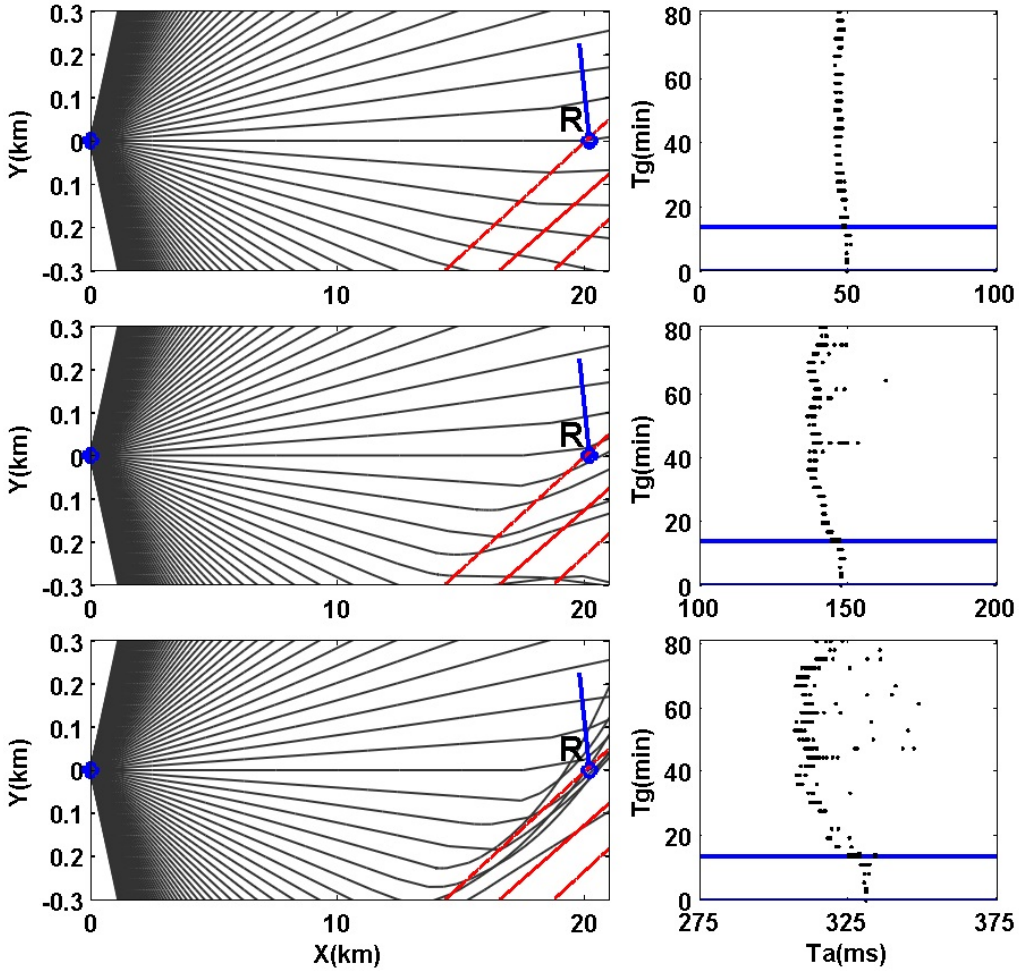

Figure 4.13: Left panel: Horizontal ray plot showing the effects of the incoming internal wave front on the propagation of vertical modes 1-3 (from top to bottom). Three red lines show the front, center, back of the incoming internal wave. Right panel: Geo-time as a function of arrival time of the first three modes (from top to bottom). The horizontal blue lines in each subplot indicate the geo-times, respectively.

source is placed at (0,0). The contour overlay shows the isotherms of the sea water, noticing the parallel lines of 17^oC and 21^oC indicating two internal waves, with the small one on top. All three modes PE results show three distinctive zones, but to a different extent. Zone 1 is the focusing around the area in front of the first front. The acoustic energy is pushed by the warm front and concentrated at this zone. Zone 2 is where the interference area with the stripe pattern. Zone 3 is the defocusing (shadow) zone at the crest of the warm water brought in by the internal wave. The acoustic energy is distributed to the both side of the wave. While it's difficult to find exact matches between the simulation results and experiment data, all three mechanisms can be found in the previous chapter. The mode-dependence described vertical-mode horizontal-ray modeling results (Fig.4.13) are also presented here. The effects of the focusing and defocusing are all intensified, and the refracted rays are bent much deeper in higher modes, resulting a broader interference zone (zone 2).

Figure 4.15 shows the efforts to match the observed acoustic mechanism using reconstructed environment. The temperature field reconstruction is limited by the coverage of on-board ship radars on R/V Oceanus and R/V Sharp, as well as the sparsity of environment moorings. Nevertheless, the reconstruction still captures the major insurgence of warm water by the internal waves and their curved nature. Each panel shows a depth-integrated acoustic intensity plot within a $20 \times 3km^2$ box. The red overlay shows the isotherm of 21^oC. At the top of each panel is the time when the environment data was gathered. Figure 4.15(A) shows that, using an reconstructed environment based on 21:33:45GMT data (water temperature and radar imagery), the interference zone is sweeping through the receiver array (short red line, marked

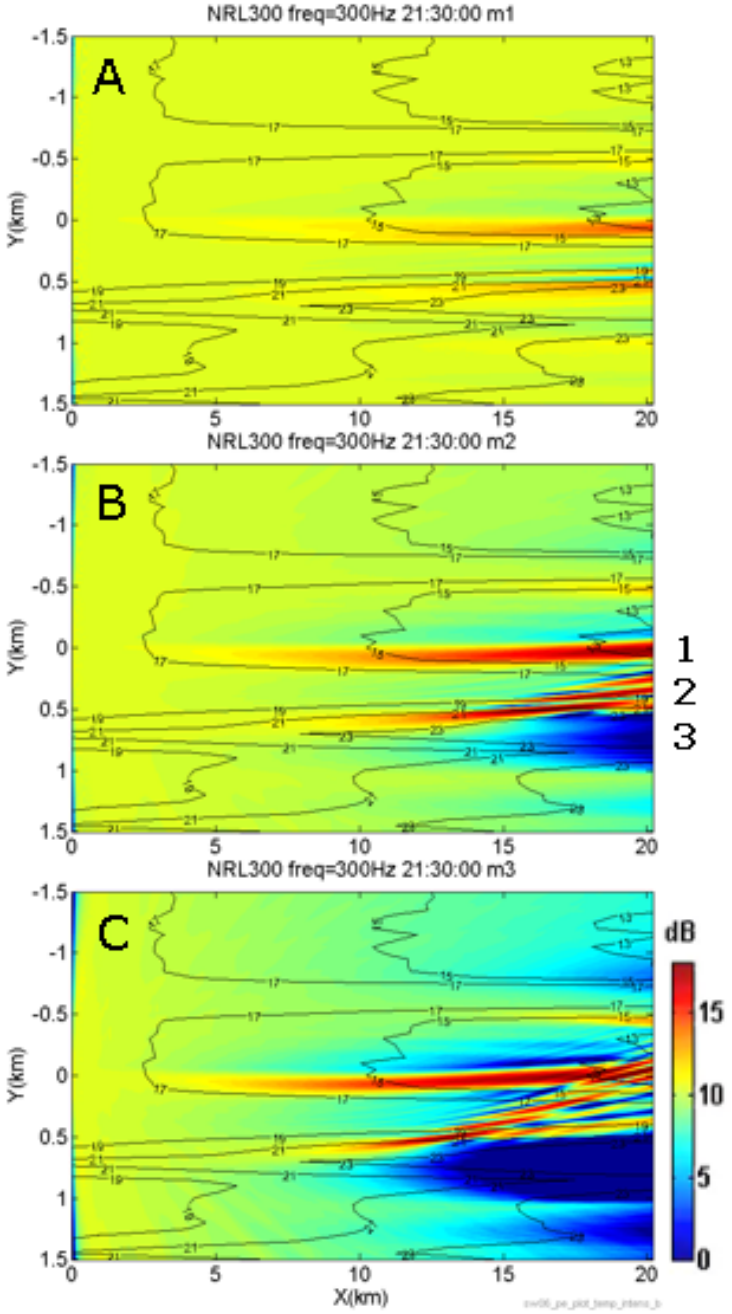

Figure 4.14: From top to bottom, PE modeling results of mode 1-3. The impacts of an incoming internal wave packet are different depending on the mode.

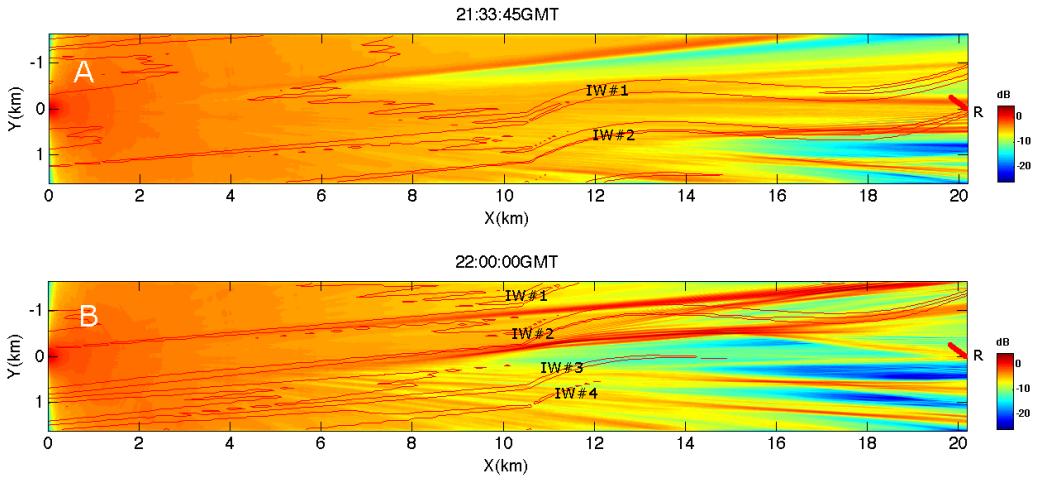

Figure 4.15: PE modeling with realistic environment matching observed acoustic mechanisms in event 50. (A) Horizontal Lloyd mirror effect using reconstructed environment. (B) Focusing/defocusing event using reconstructed environment matching observations in SW06 experiment.

"R"), matching the observations in section 4.1.2. In panel (B), while the receiver array is still siting in the shadow zone, two beams refracted back from IW#2 and IW#3 converge at the array, forming an "opportunistic" focusing event, which provides a viable explanation to the focusing in transmission 22:00-22:07 seen in section 4.1.3.

Figure 4.16 shows the comparison of the modal decomposition of experiment data (right column) and the simulated results from PE model. Although a detailed quantitative comparison is beyond the scope of this research, the comparison here still useful. It shows, the Lloyd mirror effect is impact all the modes (mode 1-3). The onset of the refract is gradual and becomes clear at around 21:32, which matches the experiment data observation. It also confirms the intensity of the effect increase with the mode number, as described

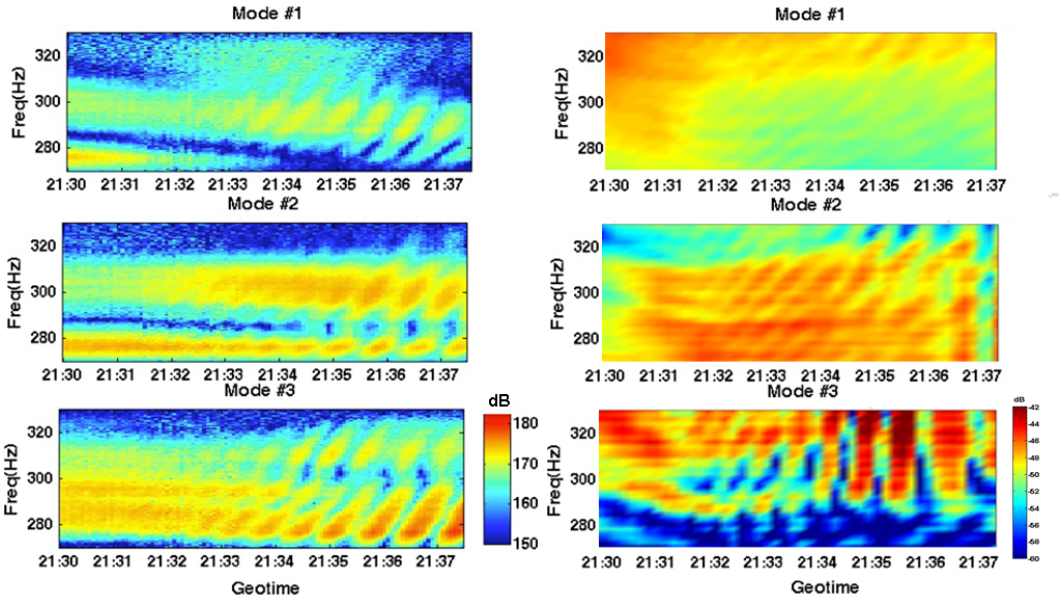

Figure 4.16: Comparison of vertical modes intensity. Left column: modal decomposition of recieved acoustic data on Shark array. Right column: PE model results of single mode propagation with realistic environment input.

in previous discussions.

Chapter 5

SUMMARY

Shallow Water 2006 experiment has provided a high quality acoustic and environmental data to investigate the acoustic wave interaction with nonlinear internal wave packets. In this thesis we have shown the problem of interaction between broadband acoustic signals in a shallow water waveguide in the presence of the horizontally propagating nonlinear internal waves (NIW). Significant acoustic intensity variations exist when NIW were passing an acoustic track with a range of about 20km between the source and receiver in 80 m water depth. Modal analysis of acoustic signals indicates a strong correlation between NIW and the acoustic signal propagation. Vertical-mode and horizontal-ray model of the waveguide in the presence of NIW reveals the cause of the intensity fluctuation is horizontal refraction when the internal wave front is almost parallel to the acoustic track. In this case, intensity focusing and defocusing occurs that can be as high as 8 to 10 dB. Numerical modeling predictions of three dimensional Parabolic Equation with input parameter reconstruction from the measured sound speed profiles during the experiment are in good agreement with the data.

One of the challenges in this research is the lack of complete 3D environment measurements. Given the limitation of the instruments, more efforts should be put on how to better design the experiment - instrument placement and how to better reconstruct environment once data is recovered. On data

processing and modeling, a 3D acoustic model with rough bottom can enable us to take bathymetry into consideration. While we have touched upon acoustic intensity fluctuation and the formation of intensity interference patterns from acoustic wave horizontal refraction, there are many other causes of the changes in the intensity that we did not address here. For example, frequency and azimuthal dependence of the sound intensity in a 3D waveguide and and spatial and temporal coherence of the acoustic waves and their relationship to the environmental parameters are potential topics for the future studies in this area.

BIBLIOGRAPHY

[1] John R Apel, Lev A Ostrovsky, Yury A Stepanyants, and James F Lynch. Internal solitons in the ocean and their effect on underwater sound. *The Journal of the Acoustical Society of America*, 121(2):695–722, 2007.

[2] J. W. Miles. "solitary waves". *Ann. Rev. Fluid Mech*, 12:11–43, 1980.

[3] L. A. Ostrovsky and Y. A. Stepanyants. Internal solitons in laboratory experiments: Comparison with theoretical models. *Chaos*, 15:037111, 2005.

[4] J. R. Apel. Linear and nonlinear internal waves in coastal and marginal seas. In M. Ikeda and F. Dobson, editors, *Oceanographic Applications of Remote Sensing*. CRC Press, Boca Raton, 1995.

[5] T. F. Duda and D. Farmer, editors. *The 1998 WHOI/IOS/ONR Internal Solitary Wave Workshop: Contributed Papers*, Technical Report WHOI-99-7. WHOI, 1998.

[6] M. Badiey, Y. Mu, J. F. Lynch, X. Tang, J. R. Apel, and S. Wolf. Azimuthal and temporal dependence of sound propagation due to shallow water internal waves. *IEEE J. Ocean. Eng.*, 27(1):117–129, 2002.

[7] M. Badiey, B. G. Katznelson, J. F. Lynch, S. A. Pereselkov, and W. Siegmann. Measurement and modeling of 3-d sound intensity variations due to shallow water internal waves. *J. Acoust. Soc. Amer.*, 117(2):613–625, 2005.

[8] Mohsen Badiey, Boris G Katsnelson, James F Lynch, and Serguey Pereselkov. Frequency dependence and intensity fluctuations due to shallow water internal waves. *The Journal of the Acoustical Society of America*, 122(2):747–760, 2007.

[9] John Lamar Worzel, Maurice Ewing, and Chaim Leib Pekeris. *Propagation of Sound in the Ocean*, volume 27. Geological Society of America, 1948.

[10] Ji-xun Zhou, Xue-zhen Zhang, and Peter H. Rogers. Resonant interaction of sound wave with internal solitons in the coastal zone. *J. Acoust. Soc. Amer.*, 90(4):2042–2054, 10 1991.

[11] J. C. Preisig and T. F. Duda. Coupled acoustic mode propagation through continental shelf internal solitary waves. *IEEE J. Ocean. Eng.*, 22(2):256–269, 10 1997.

[12] David Rubenstein and Michael H Brill. Acoustic variability due to internal waves and surface waves in shallow water. In *Ocean Variability & Acoustic Propagation*, pages 215–228. Springer, 1991.

[13] David Rubenstein. Observations of cnoidal internal waves and their effect on acoustic propagation in shallow water. *Oceanic Engineering, IEEE Journal of*, 24(3):346–357, 1999.

[14] J Luo, M Badiey, EA Karjadi, B Katsnelson, A Tskhoidze, JF Lynch, and JN Moum. Observation of sound focusing and defocusing due to propagating nonlinear internal waves. *The Journal of the Acoustical Society of America*, 124(3):EL66–EL72, 2008.

[15] Roger Oba and Steven Finette. Acoustic propagation through anisotropic internal wave fields: Transmission loss, cross-range coherence, and horizontal refraction. *The Journal of the Acoustical Society of America*, 111(2):769–784, 2002.

[16] Steven Finette and Roger Oba. Horizontal array beamforming in an azimuthally anisotropic internal wave field. *The Journal of the Acoustical Society of America*, 114(1):131–144, 2003.

[17] Timothy F Duda and James C Preisig. A modeling study of acoustic propagation through moving shallow-water solitary wave packets. *IEEE journal of oceanic engineering*, 24(1):16–32, 1999.

[18] B. Katznelson and V. Petnikov. Low frequency horizontal acousitc refraction caused by internal wave solitons in a shallow sea. *Acoustical Physics*, 46(6):774–788, 2000.

[19] J. F. andChris Emerson Lynch, Philip A Abbot, Glen G. Gawarkiewicz, Arthur E. Newhall, Ying-Tsong Lin, and Timothy F. Duda. On whether azimuthal isotropy and alongshelf translational invariance are present in low-frequency acoustic propagation along the new jersey shelfbreak. *J. Acoust. Soc. Am.*, 131(2):1762–1781, 2012.

[20] Finn B Jensen, William A Kuperman, Michael B Porter, and Henrik Schmidt. *Computational ocean acoustics*. Springer, 2011.

[21] Robert Burridge and Henry Weinberg. Horizontal rays and vertical modes. In *Wave propagation and underwater acoustics*, pages 86–152. Springer, 1977.

[22] R. A. Kropfli, T. P. Stanton L. A. Ostrovski, E. A. Skirta, A. N. Keane, and V. Irisov. Relationships between strong internal waves in the coastal zone and their radar and radiometric signatures. *J. Geophys. Res.*, 104(C2):3133–3148, Feb. 1999.

[23] J. F. Lynch, Ying-Tsong Lin, Duda, and T. F.; Newhall. Acoustic ducting, reflection, refraction, and dispersion by curved nonlinear internal waves in shallow water. *IEEE J. Ocean. Eng.*, 35(1):12–27, 2010.

[24] Peter E Holloway. A comparison of semidiurnal internal tides from different bathymetric locations on the australian north west shelf. *Journal of physical oceanography*, 15(3):240–251, 1985.

[25] John A Colosi, Robert C Beardsley, James F Lynch, Glen Gawarkiewicz, Ching-Sang Chiu, and Alberto Scotti. Observations of nonlinear internal waves on the outer new england continental shelf during the summer shelfbreak primer study. *Journal of Geophysical Research: Oceans (1978–2012)*, 106(C5):9587–9601, 2001.

[26] A. E. Newhall, T. F. Duda, J. D. I. K. von der Heydt, J. N. Kemp, S. A. Lerner, S. P. Liberatore, Y.-T. Lin, J. F. Lynch, A. R. Maffei, A. K. Morozov, A. Shmelev, C. J. Sellers, and W. E. Witzell. Acoustic and oceanographic observations and configuration information for the whoi moorings for the sw06 experiment. WHOI Technical Report WHOI-2007-04, Woods Hole Oceanographic Institution, Woods Hole, MA, 2007.

[27] M. Badiey, Y. Mu, J. Lynch, J. R. Apel, and S.Wolf. Temporal and azimuthal dependence of sound propagation in shallow water with internal waves. *IEEE J. Ocean. Eng.*, 27(1):117–129, 2002.

[28] Mohsen Badiey, Boris G Katsnelson, James F Lynch, and Serguey Pereselkov. Frequency dependence and intensity fluctuations due to shallow water internal waves. *J. Acoust. Soc. Amer.*, 122(2):747–760, 2007.

[29] Kevin L Cockrell. *Understanding and utilizing waveguide invariant range-frequency striations in ocean acoustic waveguides*. PhD thesis, Massachusetts Institute of Technology, 2011.

[30] Kevin L Cockrell and Henrik Schmidt. A relationship between the waveguide invariant and wavenumber integration. *The Journal of the Acoustical Society of America*, 128(1):EL63–EL68, 2010.